Displacement of extracellular chloride by sulfated glycosaminoglycans of the brain's extracellular matrix*

Kieran P Normoyle,[1,2] Kyle P Lillis,[1,2] Kiyoshi Egawa,[3] Melanie A McNally,[1,2] Mousumi Paulchakrabarti,[4] Biswa P Coudhury,[4] Lauren Lau,[1,2] Thomas Shiu,[1,2] and Kevin J Staley[1,2]

1. Department of Neurology, Division of Child Neurology, Massachusetts General Hospital, Boston, MA, United States
2. Department of Neurology, Harvard Medical School, Boston, MA, United States
3. Department of Medicine, Hokaiddo University, Sapporo, Hokaiddo, Japan
4. GlycoAnalytics Core, University of California San Diego, La Jolla, CA, United States

Abstract

GABA is the primary inhibitory neurotransmitter. Membrane currents evoked by $GABA_A$ receptor activation have uniquely small driving forces: their reversal potential (E_{GABA}) is very close to the resting membrane potential. As a consequence, $GABA_A$ currents can flow in either direction, depending on both the membrane potential and the local intra and extracellular concentrations of the primary permeant ion, chloride (Cl). Local cytoplasmic Cl concentrations vary widely due to displacement of mobile Cl ions by relatively immobile anions. Here we use new reporters of extracellular chloride (Cl^-_o) to demonstrate that Cl is displaced in the extracellular space by high and spatially heterogenous concentrations of sulfated glycosaminoglycans (sGAGs). Cl^-_o varies widely, and the mean Cl^-_o is only half the canonical concentration, i.e. the Cl concentration in the cerebrospinal fluid. These unexpectedly low and heterogenous Cl^-_o domains provide a mechanism to link the varied but highly stable distribution of sGAGs in the brain's extracellular space to neuronal signal processing via the effects on the amplitude and direction of $GABA_A$ transmembrane Cl currents.

Introduction

$GABA_A$ synapses comprise the primary output for inhibitory interneurons in the brain (Hu *et al.*, 2014; Tremblay *et al.*, 2016). A unique feature of $GABA_A$ synapses are the very small driving forces for ion flux through open $GABA_A$ receptor-operated membrane channels. The reversal potential for the primary permeant ion, chloride, is usually within a few mV of the neuronal resting membrane potential (RMP) (Thompson *et al.*, 1988) and may even be positive to RMP (Staley & Mody, 1992; Tyzio *et al.*, 2008). This low driving force makes possible a novel form of synaptic plasticity at $GABA_A$ synapses: the direction of current flow, i.e. the effect of $GABA_A$ receptor activation on the resting membrane potential, can be reversed by low millimolar alterations in the local chloride concentration (Coombs *et al.*, 1955). Such physiological variance is routinely observed in individual studies (Ebihara *et al.*, 1995; Huberfeld *et al.*, 2007) and is likely to underlie the 25 mV range of reported group mean reversal potentials in 20 recent studies of evoked $GABA_A$ currents recorded with gramicidin perforated patch electrodes in area CA1 of the hippocampus (tabulated in (Rahmati *et al.*, 2021). This variance has substantial effects on synaptic signaling: the reversal potential of $GABA_A$ currents evoked in a single

pyramidal cell by stimulation of 8 different presynaptic interneurons also varied by over 20 mV (Rahmati *et al.*, 2021).

We have proposed that the intracellular chloride concentration (Cl^-_i) is not monotonic across the neuronal cytoplasm, but rather varies inversely with the local concentration of macromolecular anions that comprise the vast majority of intracellular anions (Glykys *et al.*, 2014a; Rahmati *et al.*, 2021). This phenomenon is known as Donnan exclusion (Marinsky, 1985a; Helfferich, 1995; Fatin-Rouge *et al.*, 2003; Epsztein *et al.*, 2018; Gao *et al.*, 2022). Mobile ions, in this case Cl, are repelled by relatively immobile ions such as proteins with negative surface charges. Many proteins such as gephyrin that are associated with $GABA_A$ synapses bear large negative surface charges (Sola *et al.*, 2001), suggesting that variance in the $GABA_A$ reversal potential (E_{GABA}) is determined by local fixed cytoplasmic charge densities. However, E_{GABA} is not determined solely by Cl^-_i but rather by the ratio of intra- to extracellular permeant ions. This raises the possibility that spatial variance in the extracellular Cl concentration (Cl^-_o) could also be an important determinant of E_{GABA}.

The displacement of Cl^- by fixed negative charges should also occur in the extracellular space, where the high negative charge density of the polysulfated glycosaminoglycans (GAGs) that comprise the bulk of the extracellular matrix (Karamanos *et al.*, 2021) can be as high as the Cl^- concentration in the CSF (Urban *et al.*, 1979; Chahine *et al.*, 2005; Morawski *et al.*, 2015). Thus some to all of the local Cl^-_o could be displaced, depending on GAG density and the degree of GAG sulfation. Such displacement has been most clearly demonstrated in the matrix of cartilaginous tissue, where the negative charge density of the extracellular matrix can reach 400 meq / liter (Lesperance *et al.*, 1992), but dozens of mM of Cl^-_o are also displaced by sulfated GAGs in tissues such as skin (Titze *et al.*, 2004). Mucous, which comprises the extracellular space for airway epithelial cells, is also rich in polysulfated GAGs that displace about half of the Cl^-_o (Reuter *et al.*, 1998).

Many findings suggest that the brain Cl^-_o is lower than the canonical value. Xray emission spectroscopy of the extracellular space has demonstrated sulfate concentrations as high as 100 mM (Morawski *et al.*, 2015). Astrocytic buffering of Cl^-_o (Egawa *et al.*, 2013) would not be necessary if Cl^-_o were indeed > 100 mM. The gating of Group II and III metabotropic glutamate receptors, kainate receptors, acid-sensing membrane ion channels, and the transport rate of the GlyT1 glycine transporter are all strongly modulated by Cl^-_o over the entire range of 1 - 100 mM (Kuang & Hampson, 2006; Plested & Mayer, 2007; Kusama *et al.*, 2010; DiRaddo *et al.*, 2015; Tora *et al.*, 2018; Zhang *et al.*, 2021). Such strong modulation by low Cl^-_o would not make sense if Cl^-_o was uniformly > 100 mM.

Studies of Cl^-_o are few, particularly in live tissue, and have only been carried out with relatively large multibarreled ion-sensitive electrodes with tip diameters of 3-5 microns (Jiang *et al.*, 1992). This technique may alter the reported Cl^-_o via leakage of Cl from the high-Cl barrel of the electrode or distortion of the extracellular milieu through which the electrode passes. Modern Cl-selective microelectrodes are less invasive, yet recent studies also demonstrate modest variance in Cl^-_o of only a few mM (Kroeger *et al.*, 2010).

A fluorometric study of Cl^-_o would provide a noninvasive means to establish the distribution of chloride in the extracellular space. However, no suitable Cl-sensitive organic fluorophores exist, and transgenic fluorophores such as SuperClomeleon (Grimley *et al.*, 2013a) and CloPhensor (Sato *et al.*, 2017) are not distributed in the extracellular space. We therefore developed a

chloride-sensitive fluorophore (Normoyle *et al.*, 2024) from previously described organic backbones (Biwersi *et al.*, 1992b; Biwersi *et al.*, 1994) that satisfied the following criteria. First, the fluorophore should be sensitive to Cl in the range of the extracellular chloride concentration i.e., up to 100 mM; available fluorophores have been optimized for the low millimolar chloride concentrations of the cytoplasm. Second, the fluorophore should report Cl independently of the concentration of fluorophore. Ratiometric fluorophores suitable for the extracellular space do not exist, so we used **F**luorescence **L**ifetime **Im**aging (FLIM) (Kaneko *et al.*, 2004) to remove the dependence of the fluorescence emission on fluorophore concentration. Third, the fluorophore should be constrained to the extracellular space, for which dextran conjugation is optimal (Xiao *et al.*, 2008; Tønnesen *et al.*, 2018). Fourth, the fluorophore should be excited by wavelengths that are not damaging to brain tissue, i.e. below the ultraviolet range and in the visible or infrared range. Fifth, many Cl sensors are also sensitive to pH (Kuner & Augustine, 2000; Grimley *et al.*, 2013b), so a pH-insensitive fluorophore would be ideal. Finally, the fluorophore needs to be sufficiently bright so that its emission can be reliably distinguished from autofluorescence.

Here, we utilize a newly synthesized Cl-sensitive fluorophore that meets these 6 criteria to demonstrate: stable Donnan exclusion of chloride by sulfates fixed to GAG-like carbohydrate polymers; directly measured Cl^-_o of *in vitro* and *in vivo* brain tissue that is much lower than cerebrospinal or plasma chloride; a remarkable spatial variance in Cl^-_o; and, as evidence that Cl^-_o is determined by Donnan exclusion of Cl by sulfated GAGs, Cl^-_o increases after release of these sulfates by exogenous chondroitinase.

Methods

General: Chemicals were purchased from Sigma-Aldrich (St Louis, MO) unless otherwise noted. Solutions are brought up in distilled water unless otherwise noted. Standard aCSF was brought up in 18MΩ water and consisted of (in mM): NaCl 126; KCl 3.5; $CaCl_2$ 2; $MgCl_2$ 1.3; NaH_2PO4 1.2; Glucose 11; $NaHCO_3$ 15. Low chloride aCSF variant was identical except that sodium gluconate was substituted for NaCl, resulting in 10mM Cl^-. Calibration solutions were made by mixing appropriate proportions of standard aCSF with low chloride aCSF such that a chloride and gluconate sum total of 136mM was maintained while Cl^- ranged from 10 to 136mM. Colorimetric assays were read using a Wallac Victor-2 1420 spectrophotometer with a halogen continuous wave light source and spectral line filters at listed wavelength +/- 5 to 10nm. Centrifugation steps were accomplished in a tabletop Eppendorf 5417R microcentrifuge. Reflux apparatus for synthesis consisted of a recirculating cooling bath (Fisher Scientific) filled with ethylene glycol cooling a 24/40 double-lumen coiled reflux tube (Ace Glassware, Vineland, NJ) with a 500mL round bottom flask (Corning) heated with a heating mantle regulated by a timed power controller (Glas-Col #O406 and #104A PL312, respectively).

Synthesis of ABP-dextran: The process of optimizing a bright, redshifted, pH-insensitive fluorophore that is responsive to chloride concentration over a dynamic range inclusive of expected extracellular chloride concentrations is beyond the scope of this paper and has been published separately (Normoyle *et al.*, 2024). Synthesis techniques closely followed those of the Verkman group when synthesizing related compounds (Verkman, 1990; Biwersi *et al.*, 1992a) and conjugating to dextran (Biwersi *et al.*, 1992a). Briefly, N(4-***A***mino***B***utyl)***P***henantridinium (ABP) was synthesized by a reflux of equimolar amounts of phenanthridine and N(4-

bromobutyl)phthalimide in acetonitrile followed by a second reflux in 6N HCl to hydrolyze phthalate. Product was twice recrystallized from 95% ethanol before conjugation to cyanogen bromide-activated 10,000g/moL (10KDa) dextran, producing 10KDa ABP-dextran with an approximate molar labeling ratio of 4.4.

Sulfation of agarose: We modified the method of Fuse and Suzuki (Fuse & Toshiya, 1975) to add sulfate groups to the repeating disaccharide units of agarose. The goal of maximizing sulfation must be balanced with the consequent erosion of gel properties such as gelation and water holding capacity. Briefly, Agarose was added to a well-dried Erlenmeyer flask and dissolved in DMSO at a concentration of 4%(w/v) at room temperature before being cooled to 4°C with stirring. Addition of 4:1 mixture of acetic anhydride / glacial acetic acid, also pre-chilled to 4°C, was added to agarose/DMSO mixture (0.4 volumes) in 4°C coldroom. Vigorous mixing by handheld rotation was necessary to thin the gelatinous mixture to a slurry and allow stirring at 4°C for 15 minutes; gentle heat transfer from experimenter's hands helped loosen the initial gel but care is taken to return the mixture to 4°C. Sulfuric acid (15.6M) is then added slowly at a 6:1 molar ratio to agarose repeating disaccharide units, taking care to keep temperature between 4-10°C. Mixture is then moved to ambient temperature and allowed to stir for 15 minutes before reaction is stopped by neutralization with 10M NaOH after again cooling to 4°C and maintaining temperature between 4-10°C in coldroom. Sulfated agarose is then dialyzed at ambient temperature in 12-14KDa dialysis tubing (SpectraPor S432703) against 15 volumes of 50mM Tris pH 7.4 once, then against distilled water changed twice daily until dialysate clarifies. Agarose is then precipitated in 95% ethanol cooled to 4°C >4hours; over-dialysis may hinder ethanol precipitation due to a lack of sufficient counter-ion presence. Precipitate is then vacuum filtered and oven-dried at 50°C. Material is loosened with polished glass pestle and stored at ambient temperature in sealed glass vial until use. Note that careful temperature and pH control is necessary throughout exothermic processes to maintain gelation characteristics of the product.

Measurement of sulfate concentration in polysaccharide gels: $BaCl_2$-gelatin turbidimetric method (Torres *et al.*, 2021) was used to quantify the sulfate content of gel materials. Sulfated agarose product or commercially available agarose or agar powder was dissolved in 0.5M HCl at a concentration of 5% (w/v) in 2mL screw-top microtubes with gasket (Fisher Scientific). Tubes are then placed in a heat block at 100-110°C for 3hours with periodic vortex mixing, hydrolyzing the sugar backbone and releasing sulfate. All samples had varying amounts of insoluble dark brown precipitated sugar, which was clarified at 20,000 x g for 10 minutes. Standards are diluted from 1M Na_2SO_4 stock in 0.5M HCl. $BaCl_2$-gelatin reagent is freshly prepared by dissolving 30mg gelatin in 10mL distilled water at 80°C for 10minutes, then promptly adding 100mg $BaCl_2$ and vortex mixing. $BaCl_2$-gelatin is then allowed to cool passively before use. Samples are prepared by combining 1 part sample (diluted as desired), 1 part $BaCl_2$-gelatin, and 3 parts 0.5M HCl. Assay is performed in a glass-bottom 96-well plate reading absorbance at 405nm. Multiple sample dilutions were prepared and concentrations were calculated only from dilutions whose readings were well within the dynamic range of the standards.

Measurement of Cl^- in agar or agarose gels (chemical method): Chloride was measured colorimetrically using mercury(II) thiocyanate ($Hg(SCN)_2$) / iron(III) nitrate ($Fe(HNO_3)_3$) absorbance method of Florence and Farrar (Florence & Farrar, 1971) to infer Cl^- from $Fe(SCN)_3$ production through the two-step reaction,

$$[\mathrm{Hg(SCN)_2} + 2\mathrm{Cl^-} \rightleftharpoons \mathrm{HgCl_2} + 2\mathrm{SCN^-}]\mathrm{x3}$$

$$[3\mathrm{SCN^-} + \mathrm{Fe(NO_3)_3} \rightleftharpoons \mathrm{Fe(SCN)_3} + 3(\mathrm{NO_3})^-]\mathrm{x2}$$

reading $Fe(SCN)_3$ absorbance at 490nm. Briefly, agar or agarose gels cast at 5% (w/v) in 3.5cm Petri dishes were drained by gravity and then Kimwipes were used to gently wick away remaining excess fluid at sides of dish. Similar amounts of each sample are transferred to 2mL screw-top microtubes with gasket (Fisher Scientific) and 1 gel volume, estimated by weight, of 7.8M nitric acid (HNO_3) is added (final [HNO_3] = 3.9M). Samples are then placed in a heat block at 100-110°C for 3hours with periodic vortex mixing, hydrolyzing the sugar backbone to break down the gel lattice. All samples had varying amounts of insoluble dark brown precipitated sugar, which was clarified at 20,000 x g for 10 minutes. A portion of supernatant or KCl standard, diluted with 0.3M HNO_3, was combined with one-tenth volumes of 0.4M $Fe(NO_3)_3$ (in 4M nitric acid) and saturated $Hg(SCN)_2$ (in ethanol), triturated, and allowed 20minutes for reaction to reach endpoint. Stock solutions are used within 1week. Multiple sample dilutions were prepared and concentrations were calculated only from dilutions whose readings were well within the dynamic range of the standards. Final concentrations are adjusted to account for dilution from original gel sample volume.

<u>Fluorescence Lifetime Imaging (FLIM)</u>: Time-correlated single-photon counting (TCSPC) FLIM measurements were obtained using a custom laser-scanning two-photon rig driven by custom ScanImage software (MBF Bioscience, Williston, VT) equipped with a MaiTai Ti:Sapph laser (SpectraPhysics) and high-sensitivity PMT detectors (Hamamatsu C6438-01) as described previously (Normoyle *et al.*, 2024). Briefly, ABP-dextran was excited at 760nm and emitted photons were subjected to a 445/58 bandpass filter (Chroma) prior to detection using a high-sensitivity PMT. A fluorescence lifetime is calculated for each pixel by measuring the time it takes for an emitted photon to be detected, binning these photons according to arrival time, and to these data a first-order exponential equation is fit to derive the rate constant representing the fluorescence lifetime (Gehlen, 2020). The presence of a quencher will shorten fluorescence lifetime to an extent which is linearly related to quencher concentration through the Stern-Volmer equation,

$$\frac{\tau_o}{\tau_i} = 1 + [Q]k_{SV}$$

where τ_o / τ_i represents the unquenched lifetime divided by the shortened lifetime at a given quencher concentration ([Q]) (Gehlen, 2020). The Stern-Volmer constant (k_{SV}) of the resultant line relates the concentration of quencher to the shortening of fluorescence lifetime. Photons were collected over an acquisition period of 60 seconds (*in vivo* and agarose gels) to 90 seconds (*in vitro* slice cultures) and the lag between incident laser pulse and resulting photon detection recorded. The population of photons in each individual pixel is fit to an exponential to yield a lifetime value and summed to yield an intensity value using the FLIMJ plug-in for ImageJ. Further image processing, calculations, and statistics were accomplished using built-in functions and custom routines developed in Matlab (v2018b and v2022a; Mathworks, Natick, MA). For composite image generation, see *Image processing in Matlab* section below.

<u>Calibration of ABP-dextran:</u> ABP-dextran is synthesized, conjugated, and calibrated as described previously (Normoyle *et al.*, 2024). Briefly, we calibrated ABP-dextran against aCSF with varying chloride concentrations by preparing standard aCSF (in mM: NaCl 126; KCl 3.5;

$CaCl_2$ 2; $MgCl_2$ 1.3; NaH_2PO4 1.2; Glucose 11; $NaHCO_3$ 15) and a low-chloride aCSF in which NaCl was replaced with sodium gluconate. We mixed appropriate amounts of each to vary chloride concentrations (10-136mM) while maintaining the sum of sodium chloride and sodium gluconate at 136mM. Although k_{SV} values did not differ appreciably between ABP-dextran batches nor when measured using different FLIM-capable microscopes, out of an abundance of caution we used a single batch of ABP-dextran and obtained FLIM calibration parameters specific for this batch of fluorophore and the custom microscope used for all experiments reported in this manuscript. Because calibrations done in aCSF have a minimum Cl^- of 10mM as described, the unquenched lifetime (τ_o) used for Stern-Volmer calculations is approximated as the y-intercept (Cl^- = 0mM) of a best-fit curve of the raw calibration data; empirically, a biexponential fit was used. Each concentration of Cl^- in the calibration curve has a normally distributed set of ABP-dextran lifetime values with a near-constant relative standard deviation (RSD = standard deviation divided by mean) (Normoyle *et al.*, 2024). All calculations are otherwise done as described under *Fluorescence Lifetime Imaging (FLIM)* section above.

Animals: All animal protocols were approved by the Massachusetts General Hospital Institutional Animal Care and Use Committee. Wild type mice (C57bl/6; Jackson Labs 000664) of either sex were used for this study. Mouse pups remained in the home cage with the dam under standard husbandry conditions until postnatal day 6 to 8 (P6–8) when organotypic slice cultures were prepared or until a cortical window was surgically placed at P26-30.

In vitro organotypic slice cultures and imaging: Organotypic hippocampal slice cultures were prepared either as glass-mounted (Berdichevsky *et al.*, 2016) or membrane insert-mounted (Stoppini *et al.*, 1991) cultures. Briefly, in either case hippocampi are obtained from P6-8 mice and cut to 400μm thick slices. These are then gently transferred to a 6-well dish containing either a membrane insert (Millipore) or a poly-L-lysine coated coverslip (Electron Microscopy Sciences), are fed twice weekly with 1mL neurobasal-A media supplemented with 500μM Glutamax, 2% B-27, and 0.03mg/mL gentamycin (all from Invitrogen), and are incubated at 35C in a 5% CO_2 incubator. Cultures are typically imaged between DIV 12-21 in aCSF warmed to 33°C and bubbled with 95%O_2 / 5% CO_2 perfused at a rate of approximately 100mL/hour unless otherwise noted. Slices were pretreated with 500μg/mL ABP-dextran for 1-2 hours prior to perfusing with aCSF containing 136mM chloride and the same concentration of ABP-dextran. Slices were allowed to equilibrate in perfusate for 20-30 minutes before imaging, equaling at least 2 hours of total exposure to ABP-dextran prior to initiation of imaging. Two photon images were captured on a perfusion-enabled stage with a 20x water-immersion objective, NA 0.95, and analyzed as described (see *Image processing in Matlab* section below).

In vivo murine cortical window imaging: Using a modified method based on that of Che et al.,(Che & De Marco García, 2021) we placed cortical windows in young adult mice (P26-30) for acute (non-survival) imaging in accordance with Massachusetts General Hospital Institutional Animal Care and Use Committee policies and procedures (protocol 2018N000221). Briefly, anaesthetized mice were immobilized with standard ear bars and nosepiece until custom headbar is placed. A section of scalp is removed to expose a roughly 1cm section of skull. Acrylic dental cement powder (Lang Dental, Wheeling IL) mixed with cyanoacrylate adhesive is used to fix the headbar to the exposed skull at 4 o'clock to Bregma, creating a 5mm diameter working area just lateral to midline. A 2.5mm round section of skull and underlying dura is removed and a 3mm No. 1 coverslip is placed over the exposed cortex. Coverslip has 10μL concentrated ABP-dextran / agarose mixture (1%w/v low gelation temperature agarose, Sigma-

Aldrich, with 10mg/mL ABP-dextran in aCSF) pipetted from 42°C heat block immediately before inversion and placement over cortex. One hour is allowed before image acquisition for ABP-dextran diffusion into cortex from overlying agarose (between cortex and coverslip) during which time the warmed breadboard with immobilization apparatus and anesthetized mouse is transferred to the microscope table for *in vivo* imaging. This custom-made gantry-type microscope accommodates the breadboard as a stage for *in vivo* imaging. Two photon images were captured with a 16x water-immersion long focal distance objective, NA 0.80, and were analyzed as described (see *Image processing in Matlab* section below).

Agarose or agar gel Cl^- determination using ABP-dextran FLIM: Cl^- within an agar or agarose gel was measured using the two-photon rig described above in the *in vivo* section, except with a 4x (NA 0.28) objective. Using an 8-well microchamber with silicone dividing gasket (Ibidi, Grafelfing, Germany), gels were cast in aCSF containing ABP-dextran and subsequently transferred to a single Petri dish where they were equilibrated with aCSF containing ABP-dextran for at least 1 hour prior to imaging. FLIM measurements were taken as described, generally one field per quadrant at a depth of between 50-100microns. Importantly, the gasket separating gels of differing compositions was removed such that all gels in an experiment were bathed in the same aCSF with the same Cl^-. Where gels were kept for more than 1 day, they were prepared in aCSF without glucose and kept refrigerated between readings to prevent fouling.

Chondroitinase treatment of organotypic hippocampal slice cultures: Chondroitinase ABC (ChABC; AMSBIO, #E1028-02) was brought up in aCSF containing 0.1% bovine serum albumin (BSA) to a concentration of 1U/mL. Slices grown on membrane inserts were treated for 1hour either with aCSF containing ChABC or sham aCSF containing only the 0.1% BSA vehicle. Both experiment and control had 0.5mg/mL ABP-dextran (50μM), and FLIM imaging was done using the two-photon rig described in the *in vivo* section above. At the conclusion of imaging, the aCSF was collected for detection of liberated chondroitin sulfate.

Measurement of sulfated glycosamioglycans (sGAGs) liberated in aCSF: Blyscan 1,9-dimethylmethylene blue-based kit (Biocolor, #B1000) was utilized for measurement of sGAGs including chondroitin sulfate proteoglycans (CSPGs). After treatment with aCSF containing ChABC or BSA vehicle as detailed above, aCSF was collected and measured as directed against standards of bovine trachea chondroitin (Blyscan kit standard) with appropriate amounts of 10x stocks of aCSF and 0.1% BSA to obtain concentrations identical to samples. 1,9-Dimethylmethylene blue reagent absorbance is read at 650nm.

Measurement of chondroitin sulfate by liquid chromatography / mass spectroscopy (LC-MS): aCSF containing either chondroitinase or vehicle was recovered after incubation with slice (see above), volume recovered carefully noted before freezing at -20˚C, and shipped over dry ice with blinded labels for analysis. The samples were filtered using 3K MWCO spin filter units (Pall Corporation Nanosep with 3K Omega Ref: OD003C34) at 14000 RPM at 10˚C for 20minutes. The flow through containing CS disaccharides was dried in speed vac. The dried flow through were reconstituted in 200µl ultrapure distilled water (Invitrogen, Cat # 10977-015) and 100µl was dried taken for $^{12}C_6$ aniline tagging by reductive amination method (Lawrence *et al.*, 2008). Briefly, the CS disaccharides were dissolved in 17µl of $^{12}C_6$ aniline followed by addition of equal volume of freshly prepared 1 M $NaCNBH_3$ (Sigma-Aldrich) in dimethyl sulfoxide: acetic acid mixture (65:35, v/v). The reaction mixture was kept at 70°C for 45min and then transferred to

dry oven at 37°C for overnight reaction (16 h). After aniline tagging samples were dried in speed-vac for 48h to remove excess reagents. The samples were then dissolved in 17µL of LC-MS grade water (Honeywell), centrifuged at 7000g for 5min. 5µL of the sample was taken and mixed with 5µL reconstitution buffer containing known amount of internal standard (5µl of the reconstitution buffer contains, 1 µl of 10X LC-MS buffer-A (80 mM acetic acid and 50 mM dibutylamine; Sigma-Aldrich), 2 µl of $^{13}C_6$ aniline-tagged CS disaccharide internal standard mixture (20pmole each) and 2 µl LC-MS grade water. CS disaccharides were analyzed by LTQ Orbitrap Discovery (Thermo Scientific) mass spectrometry attached with liquid chromatography system (Ultimate3000, Thermo-Dionex). All disaccharides were separated on a reverse phase C18 column (1mm x 150mm, 5µm, Targa, Higgins Analytical) using buffer containing dibutyl amine as ion-pairing reagent, followed by detection of disaccharides on mass spectrometer in negative ionization mode. The chromatographic steps were: 100% buffer-A (8mM acetic acid, 5mM DBA) for 10 min followed by stepwise increase of buffer-B amount; 17% buffer-B (70% methanol, 8 mM acetic acid, 5 mM DBA) for 10 min; 32% buffer B for 15 min; 40% buffer B for 15 min; 50% buffer B for 15min; 60% buffer B for 15 min; and 100% buffer A for 10 min. Flow rate was kept at 50µL per min.

<u>Calculation of ECM sulfate lost after chondroitinase digestion</u>: In order to contextualize the Cl^-_o increase we observe after chondroitinase treatment of HOSCs, we used our HPLC-derived data and approximated HOSC volume to derive a reasonable expected Cl^-_o value for comparison. HPLC data was obtained from collected chondroitinase (or sham) digestion aCSF of a known volume. Chondroitin disaccharide concentration and sulfate content were found analytically, and a total chondroitin and total sulfate amount were calculated from mean values of chondroitin sulfate content (0.2mg/mL), sample volume (0.725mL), sulfation ratio (0.95 sulfate per disaccharide), and a monosulfated disaccharide molar mass of 481.4g/moL. Given mean HOSC thickness of 266µm and typical HOSC dimensions of 3x1.5mm, we calculate the best approximation of extracellular volume (20% of total slice volume) to be 0.293mL. The organic sulfate content lost from total ECS volume comes out to 1.65mM when assuming full-depth uniform chondroitinase digestion, or 8.8mM assuming depth-dependent digestion affecting only 50µm nearest the chondroitinase reservoir (i.e., nearest the perfusate). For comparison to measured Cl^-_o, we assume the molar relationship between sulfate lost and chloride gained to be 1:1.

<u>Image processing in Matlab</u>: ABP-dextran fluorescence lifetime is converted to Cl^-_o as described above. Composite Cl^-_o images, depicting Cl^-_o values via colormap while incorporating structural data through brightness adjustment, were produced using custom Matlab routines that apply normalized intensity data to Cl^-_o images in a manner similar to commercial FLIM software. Note that intensity images were generated by summation of photons for each pixel across 32 time bins after excitation, resulting in a higher intensity background than is typical in standard two-photon images.

Pixel exclusion: We sought to perform as little processing of either intensity or lifetime data as possible, using statistical methods to objectively exclude pixels greater than three standard deviations from the mean of either property. Any remaining pixels reflecting a fluorescence lifetime outside the calibrated range (0-150mM Cl^-), as happens in pixels with poor data quality typically due to low signal, were also excluded. More specifically, pixels were excluded if ABP-dextran lifetimes were in excess of the mean at 0mM chloride, or if lifetimes were shorter than twice the standard deviation less than the mean at 150mM (calculated from calibration data).

This yielded total objective exclusion of 0.1-0.5% of pixels in a given image, which were set to black. Subjective exclusions were done either by manually drawn regions of interest (ROI) to exclude areas of perfusate at the margins of HOSCs or large blood vessels *in vivo*, or else by image-specific thresholding to exclude low-intensity areas coinciding with apparent somatic silhouettes. All exclusions were performed prior to analysis of extracellular Cl^-_o. To ensure that somatic silhouette-defined pixels, in particular, were not a subpopulation of pixels possibly reflecting ABP-dextran in an atypical compartment (e.g., the intracellular space), multiple analyses of excluded versus included pixels were performed to confirm faithful extracellular ABP-dextran signal and appropriateness of pixel exclusion (see Results).

Neuronal tracing analysis: Where somatic borders were traced for analysis, these were not dependent upon thresholding but were traced manually where neurons within the focal plane could be confidently identified based upon morphology. Traces followed the exterior aspect of the visually apparent border between bright and dim signal (see Results). Data was linearized and is presented as the pixelwise change in Cl^-_o versus linearized distance, the latter calculated from pixel centerpoints. Comparison control data is derived by applying the same traces over calibration solution images, in which stochastic pixel to pixel differences are isolated (e.g., machine noise, Brownian motion artifact, etc).

Regions of interest (ROIs) selection: ROIs are defined using intensity images for HOSCs either as a differentiation between tissue and surrounding bath, or this plus a regular division of the field (i.e., quarters or eighths) as indicated. ROI fields containing a majority of excluded pixels (e.g., perfusate) are excluded from analysis. ROIs are defined *in vivo* as cortical regions between anatomical landmarks, such as large vessels, which are easily identified through their exclusion of ABP-dextran. ROIs are then converted to masks and applied to fluorescence lifetime or Cl^-_o images. ROIs in fields in which somatic silhouettes are evident are distinguished from ROIs that are too superficial to contain discernable silhouettes such as cellular (Layer 2/3) or acellular (Layer 1) cortical fields, respectively.

Statistics: Statistical analysis was done with Matlab 2022a, with access to statistical toolbox functions. Individual tests used and *p*-values are detailed in figure legends. Corresponding *p*-value levels are indicated within figures by asterisks and listed in figure legends. *In vivo* statistical analysis of cortical Cl^-_o was accomplished with ROI mean values, but because ROI size and number varies between groups we report mean+/-standard deviation of all analyzed pixels in addition to the ROI mean+/-standard error associated with ANOVA analysis. In the interest of transparency we elected to display violin plots of all pixels analyzed overlaid with ROI mean+/-standard error, using ANOVA analysis of the latter to determine significance of findings.

Data availability statement: All data files used to generate the figures in the paper can be found on GitHub under KieranNormoyle/NeuronalChloride2023.

Results

Non-invasive measurement of extracellular chloride using ABP-dextran: ABP is a novel Cl-sensitive fluorophore compatible with Fluorescence Lifetime IMaging (FLIM) that we have optimized to be bright, red-shifted, and sensitive to chloride concentrations through the range that would be encountered in in the extracellular space. We conjugated ABP to a 10,000 Dalton (10KDa) dextran resulting in an amine-bonded moiety (Figure 1A) that is resistant to pH changes in the physiological range (Normoyle *et al.*, 2024) and is restricted to the extracellular space (see below). We validated the ability of ABP-dextran to reliably report chloride

concentration by correlating the shortening of ABP-dextran fluorescence lifetime to chloride concentration (Figure 1B) through the Stern-Volmer relationship (Figure 1C), generating a k_{SV} of 15.9M^{-1} for ABP-dextran used in these experiments. The fluorescence lifetime of ABP-dextran is not dependent upon the concentration of ABP-dextran, only the concentration of chloride. Chloride concentration also affects ABP-dextran intensity, such that high chloride concentrations not only shorten the emission lifetime but also reduce the intensity of emission. However, the concentration of chloride can be calculated (independently of the local ABP-dextran concentration) as long as sufficient photons are collected to calculate fluorescence lifetime in a given pixel.

Sulfated agarose gels as an *in vitro* model of perineuronal space: We recently observed that differing concentrations of chloride juxtaposed to one another were stable on time scales of at least 100 minutes due to the presence of immobile anionic charges present in the neuronal cytoplasm (Rahmati *et al.*, 2021), an effect known as Donnan exclusion (Marinsky, 1985b; Helfferich, 1995; Fatin-Rouge *et al.*, 2003; Epsztein *et al.*, 2018; Gao *et al.*, 2022). We tested whether Donnan exclusion was also operative in the extracellular space as a consequence of the fixed negative charges on the sulfate moieties of the glycosaminoglycans that comprise the bulk of the extracellular matrix (Karamanos *et al.*, 2021). This matrix is most frequently visualized as the perineuronal lattice-like structures found around all neurons and first described by Golgi in 1898 (Golgi, 1898; Celio *et al.*, 1998). The process of Donnan exclusion does not require an ongoing energy input, although this issue has been contested (Glykys *et al.*, 2014b; Voipio *et al.*, 2014). We therefore modeled the brain's extracellular matrix using a reduced system to remove the possibility of active buffering of Cl^-_o by astrocytes (Egawa *et al.*, 2013) or other cellular or vascular elements. We used gels of sulfated agarose to mimic the sulfated glycosaminoglycans such as the chondroitin sulfate-decorated aggrecan family members that are prominent in the perineuronal matrix. Agarose is a nominally sulfate-free linear glycopolymer that is a major component of agar (Figure 2B; bars 1 and 2) that was used as a chemically homogenous starting material for covalent sulfate linkage. We optimized the method of Fuse and Suzuki (Fuse & Toshiya, 1975) to balance the gelatinizing properties of agarose with the dispersive, hydrophilic Donnan effects arising from incorporation of the charged sulfate groups (Gregor, 1951; Helfferich, 1995). We obtained a sulfated agarose that could be used to cast gels with 50 mM effective sulfate concentration (Figure 2B, bar 3; 49.8+/-0.9mM sulfate across three batches [mean+/-SD]) covalently linked to the polymerized agarose lattice. Gels cast from sulfated agarose serve as a simple *in vitro* model of the perineuronal extracellular space, allowing us to investigate the ability of covalently linked anions attached to a three-dimensional matrix to displace mobile chloride ions.

We measured the chloride concentrations within non-sulfated agarose gels vs. sulfated agarose gels, each equilibrated in aCSF, and compared these to the chloride concentration in the surrounding aCSF using either a standard colorimetric iron(III) thiocyanate assay (Figure 2C, dark gray bars) or ABP-dextran FLIM imaging (Figure 2C, light gray bars). Agarose gels with fixed anions in the form of covalently bound sulfate had significantly decreased chloride concentrations versus both control aCSF and non-sulfated agarose gels (Figure 2C, right pair vs left and center pairs, respectively) measured either with the standard chemical assay (dark gray bars; $p = 0.00264$ and $p = 0.00354$ by Student's paired *t*-test, respectively) or ABP-dextran FLIM (light gray bars; $p < 0.001$ by Student's paired *t*-test for either comparison). We measured a small chloride increase within non-sulfated agarose gels vs control aCSF in either assay, representing an insignificant increase when using the standard chemical assay (8.05+/-6.14mM,

mean+/-standard deviation; p = 0.190 by Student's paired t-test) and a smaller yet statistically significant increase when measured using ABP-dextran FLIM (4.95+/-0.51mM, mean+/-standard deviation; p = 0.00328 by Student's paired t-test). Later ABP-dextran FLIM experiments comparing aCSF perfusate to non-sulfated gels show no such difference (see below and Figure 2E). This Cl^- increase is curious but is quantitatively small and qualitatively distinct from the Cl^- decrease we see in sulfated agarose gels (3.5% increase from non-sulfated gel vs. aCSF control compared to a 40.7% decrease from sulfated agarose gel vs. aCSF control, respectively), meaning that any effect would be a small overestimation of Cl^- within sulfated agarose gels. The overall agreement of results derived from both assays lends confidence to the reliable performance of ABP-dextran FLIM versus standard chemical colorimetric methods of Cl^- measurement.

Next we placed separately cast non-sulfated and sulfated gels adjacent to each other and equilibrated in the same aCSF bath with ABP-dextran (Figure 2D; schematic in Figure 2A). ABP-dextran FLIM measurements of chloride concentration within the non-sulfated and sulfated gels demonstrated significant chloride concentration differences between gels that had no fixed anionic charge to displace mobile chloride (non-sulfated agarose; Figure 2D light blue bars) vs. gels that had covalently bound sulfate groups (sulfated agarose; Figure 2D dark blue bars). The chloride concentrations were inversely proportional to the sulfate concentration in the gel, were significantly lower for sulfated gels at each time point (each $p < 0.001$), and were stable for over three weeks (agarose gel comparisons: each p = 1.0000; sulfate gel comparisons: 2-4hours vs 24hours p = 1.0000, 3weeks vs 2-4 hours and 24 hours p = 0.211 and p = 0.113, respectively; ANOVA with Bonferroni correction). These findings support the displacement of mobile chloride ions by the sulfates fixed to the gel (Figure 2D) by Donnan exclusion. We next imaged both non-sulfated and sulfated gels immediately juxtaposed to one another, along with aCSF perfusate, in the same field (Figure 2E) and demonstrated that the presence of sulfate groups covalently bound within the polymerized gel results in a significantly decreased chloride concentration relative to both non-sulfated gels and aCSF perfusate (Figure 2E, bar 3 vs bar 2 and bar 1, respectively; each $p < 0.001$ by Student's paired t-test). Non-sulfated agarose gels demonstrated no difference versus aCSF perfusate (p = 0.0647 by Student's paired t-test).

<u>Demonstration of chloride displacement in living systems:</u> To test whether Donnan exclusion is also operative in the extracellular matrix of the brain, we studied mouse hippocampal organotypic slice cultures. We tested whether extracellular perineuronal fixed anions, such as the chondroitin sulfate moieties of aggrecan family proteoglycans (Frantz *et al.*, 2010; Karamanos *et al.*, 2021), displace chloride in this living system. After incubation with ABP-dextran and equilibration with aCSF containing ABP-dextran and 136mM chloride, we measured extracellular chloride concentration using ABP-dextran FLIM and found that Cl^-_o was unexpectedly low and heterogenous (46.7 +/- 18.8 mM, calculated from 25.8×10^6 pixels across 32 fields of 7 slices). Representative fields are shown in Figure 3A (ABP-dextran intensity) and Figure 3B (Cl^-_o composite image, quantified in Figure 3C). Paired analysis of slices pre- and post-ABP-dextran incubation confirmed that autofluorescence signals in pixels in pre-ABP images did not contribute to the unexpectedly low values of Cl^-_o obtained from post-ABP images. This is because pre-ABP pixels that had both sufficient photon count to allow lifetime calculation and lifetimes within the calibrated range of ABP-dextran had short lifetimes whose effect would be to increase the reported Cl^-_o, not decrease it.

Perineuronal traces along the outer edge of neuronal silhouettes (Figure 3B, white dashes) were used to analyze the spatial change in Cl^-_o in the extracellular space immediately adjacent to the neuronal cytoplasmic membrane. Pyramidal neuron silhouettes were identified morphologically and pixels underlying the extracellular margin (i.e., perineuronal) traces were linearized for analysis. We compared the size of the effects of fixed anions on local Cl^-_o to Brownian and machine noise arising from FLIM of ABP-dextran in bulk solutions with similar mean Cl^-_o. The pixel-to-pixel change in Cl^-_o (ΔCl^-_o) versus distance in the presence of fixed anions in the perineuronal space (Figure 3D, blue) was much larger than the ΔCl^-_o versus distance in the absence of fixed anions in bulk solution containing ABP-dextran and a single concentration of Cl^- (Figure 3D, red). Figure 3E shows similar data for a larger cohort of perineuronal tracings and their corresponding aCSF solution counterparts (N = 72). We found a consistently increased probability of greater ΔCl^-_o per micron in the extracellular space where fixed extracellular anions were present compared to the perfusate aCSF (Figure 3E, blue vs red).

We further analyzed dim pixels typical of the neuronal silhouettes, which had not already been statistically excluded and displayed as black. These dim pixels retain their Cl^-_o colormap values but are often so dim they are difficult to appreciate visually (e.g., Figure 3B). They are included in presented images in the interest of transparency but were excluded from Cl^-_o analysis after applying an empirically derived threshold value that best approximates the clearest silhouettes in each image. We reasoned that these pixels represented photons originating from extracellular ABP-dextran above or below the focal plane, likely present due to the higher-background FLIM-derived intensity images (Figure 4A) which represent a summation of all photons in each pixel. Because Cl^-_o is derived from the intrinsic, intensity-independent property of fluorescence lifetime, structural context is lost in Cl^-_o images (Figure 4B) and must be reestablished by incorporation of intensity information into a composite image (Figure 4C). This is not unique to Cl imaging; commercial FLIM software creates intensity-lifetime composite images in a similar manner. In our images we first converted from fluorescence lifetime to Cl^-_o to allow the use of a linear colormap for readers' ease of interpretation (see Methods).

The dim, excluded pixels occurring in neuronal silhouettes offered an opportunity to assess whether they were in fact out-of-focus, extracellular ABP-dextran. If true, this would produce a similar, if wider (Normoyle *et al.*, 2024), distribution of Cl^-_o values. Conversely, if the dim, excluded pixels were autofluorescent in origin or were reflective of low Cl^-_i reported by ABP-dextran leaked into neurons, then we would find a right-shifted, high-Cl^-_o distribution or a left-shifted, low-Cl^-_o distribution, respectively.

<u>Verification of ABP-dextran extracellular compartmentalization:</u> We used two approaches to assessing the Cl values reported in the dimmest pixels. We first compared all pixels below the exclusion threshold to all pixels above the threshold. Only pixels outside the actual slice (i.e., perfusate pixels) and those pixels with lifetimes outside the calibrated range of ABP-dextran were not considered. We found that included and excluded pixels had histograms with similar characteristics, such as mean and mode, although excluded pixels were fewer in number and had a wider distribution (Figure 4D, blue vs gray). There is neither a high-Cl^-_o peak indicative of autofluorescence nor is there a low-Cl^-_o peak indicative of intracellular signal in either included pixels or excluded pixels. Notably, there are virtually no included pixels in the typically intracellular range (i.e., ≈15mM Cl^-), and such pixels are far more likely to be excluded from analysis (Figure 4D, gray arrow). We conclude that intensity-excluded pixels are not a low- or

high-Cl^-_o subset, which would seem to preclude errant Cl^-_i signal. However, we wanted to rule out any possible non-extracellular signal more specifically as most pixels at these resolutions are expected to contain a portion of both neuropil and extracellular space.

As a second means to evaluate the Cl values reported in the dimmest pixels, we assessed pixels within individual somatic silhouettes. Visually apparent somatic edges are ideal to compare extracellular ABP-dextran signal in the bright perineuronal exterior of silhouettes to ostensibly intracellular pixels inside the silhouette margins. The fact that the brightest of these pixels are located nearest the outer silhouette margin and the least intense pixels are located toward silhouette centers supports our hypothesis that this signal is extracellular in origin from outside the focal plane. Alternatively, if ABP-dextran leaked inside cells, despite its conjugation to 10KDa dextran, we would expect that such an intracellular signal would be brightest in the silhouettes formed by cells firmly within the focal plane (i.e., with the most ABP-containing cytoplasm in the focal plane). After the objective pixel exclusion step (intensity greater than three standard deviations from the mean, or lifetime outside the calibrated range), we compared Cl^-_o in the perineuronal margin within one micron external to the traced border to those pixels inside the traced border. In this way our analysis was restricted to only those cells morphologically identified as pyramidal neurons adequately centered in the focal plane. Pixels from inside the silhouette are greater in number than perineuronal extracellular pixels in this analysis, yet we saw no subpopulation of intracellular chloride values (i.e., in the range of 15mM Cl^-) that would be expected if this signal were originating from 'leaked' intracellular ABP-dextran (Figure 4E). Signal from the one micron external to the perineuronal perimeter is five times as bright on average as pixels from within the silhouette (Figure 4F), which helps explain why the excluded intracellular signal has a wider distribution of Cl^-_o values (Normoyle *et al.*, 2024). If no intracellular leakage of ABP-dextran can be detected even within in-focus neuronal somatic silhouettes, where such signal is expected to be strongest if it were present, one can infer that neuropil will not contribute any such signal in pixels containing both neuropil and extracellular space. While we look forward to future experiments with greater spatial resolution, we conclude that neither objectively excluded pixels nor those excluded by intensity thresholding are indicative of low- or high-Cl^-_o subsets. Further, we provide ample evidence supporting the fidelity of ABP-dextran in its reporting of chloride exclusively in the extracellular space.

<u>Demonstration of chloride displacement by chondroitin sulfate:</u> We then confirmed that fixed anions, including chondroitin sulfate glycoproteins, are a significant contributor to this difference by measuring Cl^-_o before and after treatment with chondroitinase. Analogous to matrix metalloproteases, chondroitinase is a bacterial enzyme that cleaves the sulfated glycopolymer chondroitin. Chondroitinase treatment significantly increased Cl^-_o in organotypic hippocampal slice cultures (Figure 5A&B; pre- and post-digestion, respectively). Cl^-_o increased on average 8.3+/-3.3mM (mean+/-standard deviation) in freely diffusible extracellular chloride within the slice culture (Figure 5A vs 5B; quantified in 5D-F) and was significantly greater in chondroitinase digested slices than in sham digested slices (Figure 5B vs 5C; quantified in 5F). This increase in Cl^-_o coincides with a significant decrease in the extracellular fixed anions within the slice culture. The actual decrease in fixed anion concentration in the extracellular space was estimated from the concentration of polysulfated chondroitin released into the perfusate after chondroitinase treatment (Figure 5G) and confirmed by HPLC analysis (Figure 5H). We approximated an expected Cl^-_o increase using HPLC-derived measurements of sulfated chondroitin disaccharide and HOSC volume (see Methods). Our own empirical observations, in agreement with others' observations (e.g. Orlando and colleagues, especially Figure 5C therein)

(Orlando *et al.*, 2012) indicate that chondroitinase activity decreases with distance from its diffusive reservoir and full activity is restricted to an estimated 50μm; as such we only measure Cl^-_o to a depth of 50μm. If all digested chondroitin sulfate indeed came from only the most superficial 50μm of our HOSCs, the Cl^-_o increase expected in this same superficial 50μm is calculated to be 8.8mM. This agrees well with experimental mean Cl^-_o values calculated from regular subfields of pre- and post-chondroitinase digestion, 8.8mM versus 8.3+/-3.3mM (Figure 5E), or when using the full field to calculate the minimum and maximum range of Cl^-_o increases from 0.6-16.1mM (Figure 5D; pre-digestion mean- standard deviation to post-digestion mean+ standard deviation). Further, we find that even if we assume chondroitin sulfate is lost uniformly from the full thickness of the HOSC and recalculate a smaller expected Cl^-_o increase of 1.65mM, this still lies within the empirically measured range of 0.6-16.1mM. These observations are consistent with the expected inverse relationship between fixed extracellular anions such as sulfate and mobile Cl arising from Donnan exclusion. It would be advantageous to similarly estimate a predicted Cl^-_o based upon local sulfate concentrations and compare this to empirical Cl^-_o measurements similar to our sulfated agarose experiments (Figure 2E), but without direct and independent measurement of the extracellular sulfate content of HOSCs this is not currently feasible. In summary, the immobile ions associated with the extracellular matrix displace mobile anions such as chloride consistent with the well-established effects of Donnan equilibrium forces, such that Cl^-_o is much lower and less uniform than would otherwise be expected.

<u>Chloride displacement in the perineuronal space *in vivo*</u>: To test whether Donnan exclusion of Cl^-_o by sulfated GAGs was significant *in vivo*, we performed live 2 photon imaging of P26-30 mice via a cortical window (Figure 6A). Direct application of high concentrations of ABP-dextran into the non-sulfated agarose overlying the neocortex (Figure 6B) resulted in a robust ABP fluorescence signal from the extracellular space of the brain parenchyma. Control measurements were obtained from the agarose above the cortex, which had been brought up in aCSF (136mM Cl^-) and allowed to equilibrate with *in vivo* CSF. Notable exclusion of ABP-dextran fluorescence emission from blood vessels (Figure 6C,D&F) and cell bodies (Figure 6C) was observed. Areas of locally elevated Cl^-_o and overall bright signal seen in HOSCs (Figures 3-5) were absent *in vivo* (Figure 6), suggesting these features are specific to *in vitro* preparations. At several microns in size, we reason the areas seen in HOSCs are most likely damaged areas where intracellular space makes up less than the typical 80% of volume allowing ABP-dextran access to a greater proportion of volume, so that the signal is bright despite quenching by the high Cl^-_o in these spaces. ECM damage would also be likely in such circumstances and would be expected to result in a loss of extracellular immobile anions, limiting the Donnan exclusionary force and leading to relatively high concentrations of Cl^-_o. This combination would be expected to result in a paradoxically bright, short-lifetime ABP-dextran signal yielding an unusually intense high Cl^-_o area. Given the absence of these features *in vivo*, we speculate that these areas are the result of slicing trauma but longitudinal studies will be needed to adequately categorize them. Regions of interest (ROIs) were defined using intensity images before rendering composite images so that only structural information was considered; an example intensity and composite image pair can be seen in Figure 6D&F. Cortical Cl^-_o was less than half the chloride concentration measured in the overlying agarose (48.1 +/- 17.0mM, calculated from 68 ROIs and 4 animals, vs 135.4 +/- 5.0mM in agarose between cortex and coverglass). Cl^-_o in cellular and acellular fields displayed in Figure 6CD&F were not significantly different from each other (Figure 6E entries 2&3, respectively), nor were either significantly different from all ROIs collected from this animal (entry 4) or from all animals (entry 5; each $p = 1.0000$ by ANOVA with

Bonferroni correction), while all were significantly different when compared to aCSF measured above the cortex (each $p < 0.001$ by ANOVA with Bonferroni correction). Regional mean Cl^-_o values were approximately 45-55mM (Figure 6E) but there was notable spatial variation between regions and even within regions, similar to *in vitro* HOSC results and consistent with local Donnan exclusion of Cl^-_o by variably sulfated GAGs. Future experiments will be optimized for higher resolution imaging, but our results suggest that the well-established heterogeneity of sulfation patterns around neurons represent a means by which neurons and supporting cells can indirectly modulate Cl^-_o through Donnan forces in a manner similar to how cytoskeletal components, in particular actin, have been recently shown to influence local intracellular Cl^-_i (Rahmati *et al.*, 2021).

Discussion

We demonstrate stable Donnan exclusion of chloride by fixed anions in a transport-free system of sulfated agar using FLIM of a novel fluorophore, ABP-dextran, and validate these measurements with direct chemical assays of sulfate and chloride (Figure 2). FLIM of ABP-dextran demonstrated that Cl^-_o in the brain is less than half the Cl concentration in the cerebrospinal fluid and plasma (Figures 3-6). This low Cl^-_o arises from Donnan exclusion of chloride by fixed sulfated glycosaminoglycans (sGAGs), because release of sGAGs by chondroitinase results in an increase in Cl^-_o that varies with the amount of sulfates released (Figure 5). Major findings are confirmed *in vivo* (Figure 6).

Limitations of this study

The finding that Cl^-_o is much lower than expected in the extracellular space of living brain tissue is based on FLIM of a new Cl-sensitive fluorophore, ABP-dextran. These results are in contrast to the higher values measured using ion sensitive electrodes (Jiang *et al.*, 1992; Kroeger *et al.*, 2010). The ABP-dextran fluorophore is based on a validated structure (Biwersi *et al.*, 1992a; Biwersi *et al.*, 1992b) and was calibrated against Cl, other anions, and direct chemical analysis of chloride concentrations in situ. ABP-dextran FLIM accurately reported Cl values in sulfated carbohydrate polymers (Figure 2), so it is unlikely that the sGAGs or other anions in the extracellular environment (Figure 1C) affected the accuracy of the ABP-dextran FLIM. ABP-dextran overcomes several barriers to accurate measurement of extracellular chloride, including sufficient sensitivity in the relevant range of chloride concentrations, competition with autofluorescence, and permeation into the cytoplasmic space, where lower chloride values would be encountered. ABP-dextran was clearly excluded from the intracellular space (Figure 3A&B; Figure 4A&C; Figure 6C) and blood vessels (Figure 6C,D&E). We speculate that the difference between our novel fluorophore-based measures and the ion-sensitive electrode measures of Cl^-_o could arise from distortion of the extracellular milieu created by the stab wound of the microelectrode, although our imaging techniques do not provide sufficient spatial resolution to test this possibility. Alternatively, microelectrode-based chloride measurements may be increased by electrode solutions leaking from the high-chloride barrel of the ion-sensitive micropipette into the extracellular space (Figure S1). A study comparing fluorometric and microelectrode techniques would benefit greatly from an ABP-based ratiometric chloride sensor, currently in development (Normoyle *et al.*, 2024), and higher-resolution imaging.

Stable Donnan exclusion

An important finding in this study is that Cl microdomains established by Donnan exclusion are stable for weeks, and do not require active transport to be maintained (Figure 2). This

phenomenon is well-established in biophysics (Epsztein *et al.*, 2018; Gao *et al.*, 2022), but is more confusing in neuronal physiology where membranes with time-varying ionic permeabilities and transporters create a more complex environment (Voipio *et al.*, 2014; Doyon *et al.*, 2016; Düsterwald *et al.*, 2018; Rahmati *et al.*, 2021). A point of particular confusion is the role of active Cl transport vs. Donnan exclusion in maintaining a particular E_{GABA} in the face of GABA-gated Cl flux that alters the local Cl concentration. After a GABA-gated Cl influx, and re-establishment of local charge balance by cationic flux via voltage- and ligand-gated cation channels, the local cytoplasm will contain excess chloride salts. This Cl has two fates: either excess salt diffuses through the cytoplasm to re-establish a new equilibrium with fixed charges, or the excess salt is transported back across the membrane by cation-chloride cotransporters (Brumback & Staley, 2008; Lewin *et al.*, 2012; Doyon *et al.*, 2016; Beckstein & Naughton, 2022). The transporters are required to re-establish the original steady state volume, but in the absence of transport, diffusion maintains local Cl concentrations remarkably well (Brumback & Staley, 2008; Rahmati *et al.*, 2021). In the absence of membrane Cl salt transport, this diffusion of excess Cl salts will be associated with either a cytoplasmic volume increase from associated water influx or an increase in the mean Cl concentration in the cytoplasm. At pathologically high rates of Cl influx, membrane chloride salt transport becomes rate-limiting (Staley & Proctor, 1999; Jedlicka *et al.*, 2011; Lewin *et al.*, 2012; Doyon *et al.*, 2016), and chloride concentrations become sufficiently labile to depolarize E_{GABA} (Barker & Ransom, 1978; Alger & Nicoll, 1982; Huguenard & Alger, 1986; Staley *et al.*, 1995). Thus Donnan exclusion *establishes* the local value of E_{GABA}, and active transport *maintains* that value (and neuronal volume) in the face of synaptic Cl flux (Glykys *et al.*, 2014a). The same principals should apply to the local extracellular chloride concentrations described here, with astrocytic chloride buffering (Egawa *et al.*, 2013) and diffusion between the extracellular fluid, the CSF, and vascular spaces (Rasmussen *et al.*, 2022) taking the place of neuronal membrane cation-chloride cotransport.

<u>Low extracellular Cl</u>

The Cl^-_o measured by ABP FLIM is less than half of the canonical Cl^-_o. Such a low value of Cl^-_o should affect not only E_{GABA} but also the inhibitory $GABA_A$ conductance, because there are only half as many ions to carry the outward membrane currents (i.e. inward Cl- flux) (Coombs *et al.*, 1955). Shouldn't such a low value of Cl^-_o have been obvious from electrophysiological studies? E_{GABA} is determined by the ratio of Cl^-_i to Cl^-_o (Coombs *et al.*, 1955; Staley, 2023). If either concentration is known, the other can be determined from E_{GABA}. However if both Cl^-_i and Cl^-_o are determined by the concentrations of local immobile anions, neither can be set experimentally and thus E_{GABA} cannot be used to determine either Cl^-_i or Cl^-_o; only the ratio can be inferred from the Nernst equation. Similarly, although the conductance of inward Cl flux (outward membrane current) is determined in part by Cl^-_o, it is also determined by the $GABA_A$ permeability, i.e. the number of open membrane channels and their capacity for ion flux. Thus membrane currents are not sufficient to determine Cl^-_o (Coombs *et al.*, 1955). Control of the ionic milieu is greater in single-channel recordings, but whether the complement of immobile anions is physiological under these conditions is difficult to determine, and even in these conditions there is substantial uncertainty regarding local ionic concentrations (Li *et al.*, 2015).

<u>Cl^-_o microdomains</u>

The extracellular matrix of the brain is often depicted as perineural nets surrounding parvalbumin neurons that are detected by specific agglutinins and antibodies (Celio & Blümcke, 1994). However, these assays detect very specific motifs of glycosaminoglycan sulfation; using

more permissive ionic methods, a highly anionic extracellular matrix can be seen to surround virtually all neurons (Golgi, 1898; Glykys *et al.*, 2014a; Morawski *et al.*, 2015). This extracellular matrix fills the extracellular space, which comprises about 20% of the brain's volume (Syková & Nicholson, 2008; Tønnesen *et al.*, 2018). The sGAG moiety of proteoglycans are the primary constituent of extracellular matrix (Tønnesen *et al.*, 2018; Karamanos *et al.*, 2021). GAGs are polymers of widely varied length comprised of sugars and substituted sugars (N-acetylglucosamine, glucuronic acid, and galactose) that are synthesized without templates. Up to 3 sulfates are added to the sugar moieties before export to the extracellular space. This enables the creation of a stable but highly variable spatial distribution of dense, fixed anionic charge in the extracellular matrix. Figure 3 demonstrates that this variance is substantial at the level of resolution of light microscopy. However, the distribution of fixed anions at the extracellular face of $GABA_A$ receptors, and the corresponding Cl^-_o, is currently unknown.

<u>Physiological implications</u>

Cl^-_o microdomains in the region of the extracellular openings of $GABA_A$ receptor-operated channels are a critical determinant of both E_{GABA} and the $GABA_A$ conductance. The wide range of Cl^-_o values established via Donnan exclusion by sulfated GAGs (Figures 2, 3, 4, 5 and 6) makes possible a substantial variety of effects of $GABA_A$ receptor activation based on the direction of chloride flux. These effects range from hyperpolarizing inhibition through shunting inhibition through excitation by activation of low threshold calcium currents and removal of the magnesium block of the NMDA receptor. In addition, the effects of Cl^-_o on the quantity of charge that is carried by $GABA_A$ membrane currents (the conductance) (Coombs *et al.*, 1955) makes possible a broad range of strengths of $GABA_A$ synapses that is independent of the number or subunit composition of receptors or their posttranslational modifications.

The turnover of the macromolecules comprising the extracellular matrix is very slow (Tsien, 2013), on the order of months to years based on rodent experiments (Margolis & Margolis, 1973) as well as the rate of deterioration of patients with genetic defects of GAG catabolism (Héron *et al.*, 2011; Hampe *et al.*, 2020; Seo *et al.*, 2020). This slow turnover provides a mechanism for long-lasting influences on synaptic GABA signaling. Some elements of GAG synthesis are activity dependent (Sidharthan *et al.*, 2013), but currently nothing is known about the insertion of GAGs into the extracellular matrix, in situ modification, and the capacity for directed alterations of Cl^-_o microdomains in the regions of $GABA_A$ receptors and synapses. Thus the role of extracellular chloride microdomains in synaptic signal processing and memory remains to be discovered.

<u>Pathological implications</u>

Cytotoxic cerebral edema: If Cl^-_o is normally only half of the value of Cl in CSF and plasma, then the capacity for Cl^-_o to increase acutely may be an important and hitherto unappreciated element of the pathophysiology of cerebral edema (Glykys *et al.*, 2017). Matrix metalloproteinases (MMPs) are released and activated after neuronal injury and death (Zhang *et al.*, 2016). Release of sulfates in sGAGs from the extracellular matrix would reduce the Donnan exclusion of Cl by fixed sulfates. This would result in an acute increase of Cl^-_o as in Figure 4. The action of equilibrative cation-Cl cotransporters would then lead to a corresponding increase in chloride salts in the cytoplasm of neighboring healthy neurons, with attendant volume increases. This novel mechanism of cytotoxic edema could potentially be ameliorated by pharmacological MMP inhibition. Alternatively, inhibition of the influx of chloride

salts that cross the BBB from the vascular space (Jha *et al.*, 2019) would limit the influx of Cl into the extra and intracellular spaces.

Post Traumatic Epilepsy: Richard Miles and colleagues demonstrated that $GABA_A$ receptor activation could be excitatory in human brain tissue resected for control of medically intractable epilepsy (Cohen *et al.*, 2002). However, the pathomechanism has never been elucidated (Huberfeld *et al.*, 2007; González, 2016; Karlócai *et al.*, 2016). Gliosis is the most common finding in medically intractable epilepsy (Thom, 2014). In glial scars, reactive astrocytes synthesize new matrix elements (Roll & Faissner, 2014; Song & Dityatev, 2018). If the replacement matrix was more heavily sulfated than the original, as would be expected from the firm texture that is responsible for the name “scar” (Lesperance *et al.*, 1992), then in areas of gliosis Cl^-_o would be low. Low Cl^-_o could contribute to degradation of $GABA_A$ receptor mediated inhibition, frank excitation, and failure of anticonvulsants whose action are predicated on intact synaptic inhibition. Thus replacement of the extracellular matrix and distortion of extracellular chloride microdomains could comprise an important mechanism of medically intractable epilepsy after brain injury.

<u>Future studies</u>

The findings that Cl^-_o is both lower than expected and spatially heterogenous opens the door for many investigations into the mechanisms by which Cl^-_o is set, such as the synthesis, export, and in situ modification of sulfated GAGs. The activity dependence of these mechanisms and the effect of Cl^-_o microdomains on synaptic signaling are additional areas of investigation. Pathologically, the impact of changes in Cl^-_o in both acute edema and long-term complications such as epilepsy may provide much-needed therapeutic insights into these frequently-intractable conditions.

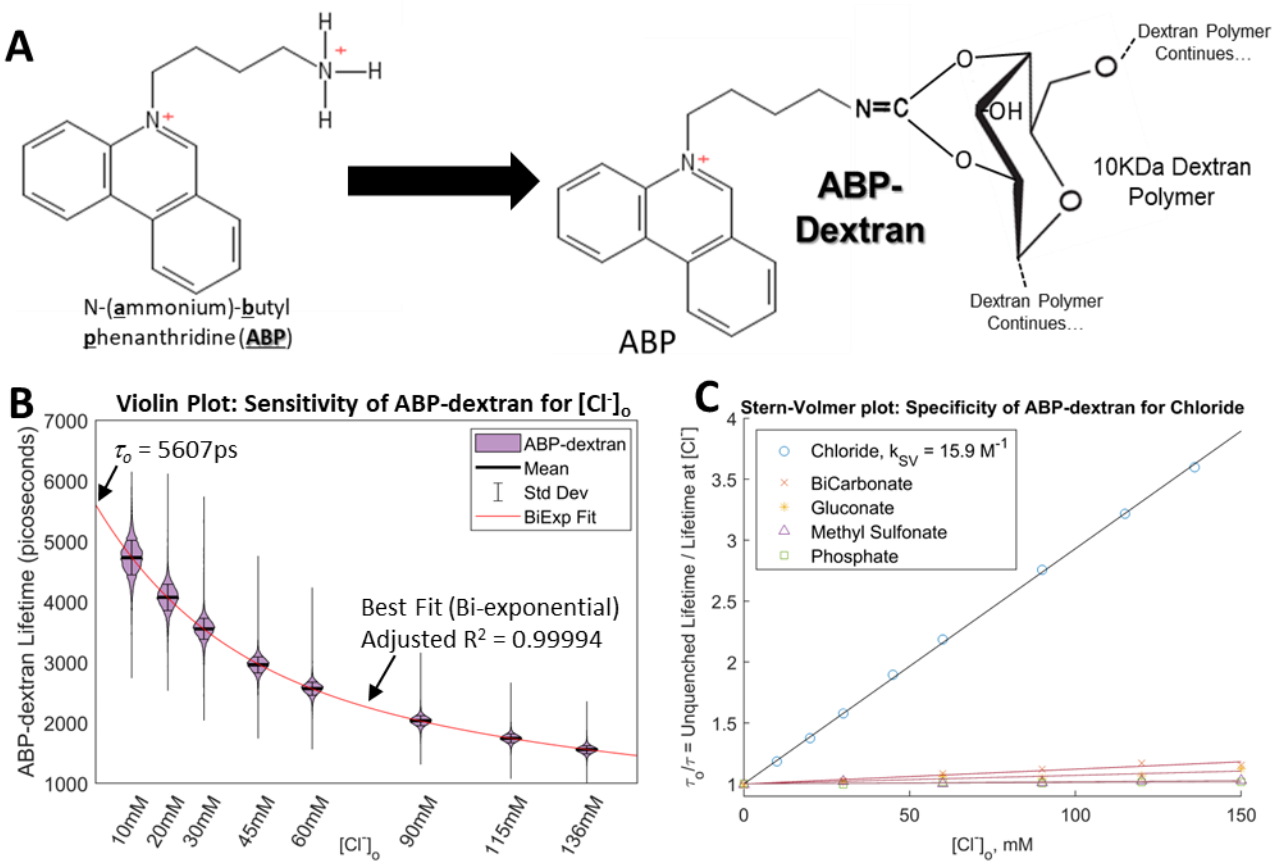

Figure 1 Characterization and Calibration of Chloride-Sensitive Fluorophore ABP. ***A)*** N-(**a**mmonium)-**b**utyl **p**henanthridine (ABP) is synthesized in-house and conjugated to activated dextran, a glucose polymer, at a ratio of 10-14 fluorescent molecules per 10KDa Dextran. ***B)*** Representative calibration of ABP-dextran fluorescence lifetime versus Cl^- demonstrating ABP-dextran sensitivity to chloride-induced quenching. Calibration of ABP-dextran fluorescence lifetime vs Cl^-_o is displayed as a violin plot with mean +/- standard deviation overlaid. ABP-dextran lifetime at 0mM chloride (t_o) is extrapolated using a best-fit approach (see Methods). ***C)*** Stern-Volmer plot demonstrates a linear relationship between ABP-dextran fluorescence lifetime and concentration of chloride and was used to convert lifetimes to chloride concentrations. The ratio of unquenched ABP-dextran fluorescence lifetime (t_o) to ABP-dextran lifetime at a given concentration of quencher (t) is plotted versus concentration of quencher (t_o/t vs $[Q^-]$). The slope of the linear regression is the Stern-Volmer constant (k_{SV}) which allows conversion of ABP-dextran lifetime to concentration of quencher, specifically Cl^- (blue circles / black line; k_{SV}=15.9M^{-1}). Four biologically relevant anions were found to have no experimentally relevant effect on ABP-dextran fluorescence lifetime: bicarbonate (k_{SV}=1.21M^{-1}), gluconate (k_{SV}=0.70M^{-1}), methyl sulfonate (k_{SV}=0.18M^{-1}), and phosphate (k_{SV}=0.11M^{-1}). Gluconate was subsequently used as a chloride substitute in non-standard aCSF formulations used for calibrations.

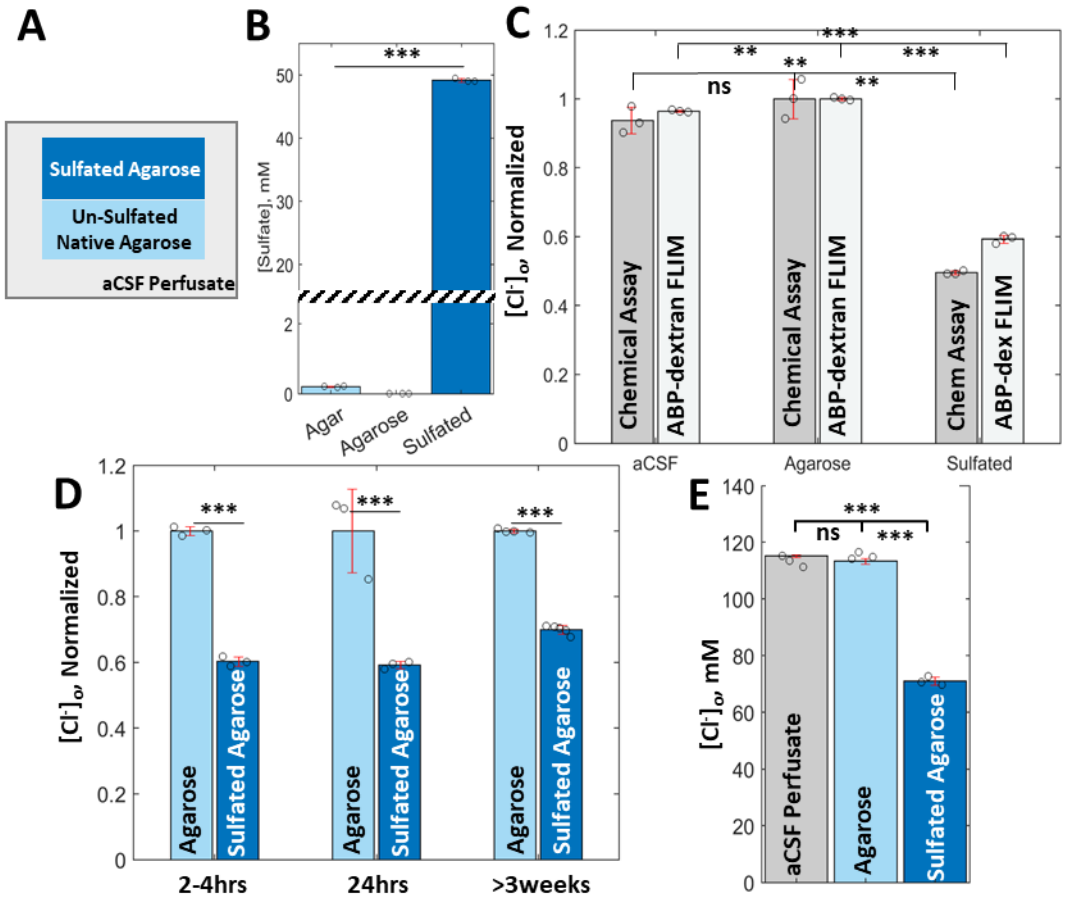

<u>Figure 2</u> Effects of immobile sulfate on Cl^- in a volume of agarose gel. ***A)*** Experimental schematic demonstrating how polysaccharide gels, cast in aCSF separately, were equilibrated in aCSF after transfer to a common vessel. Gels were either equilibrated with aCSF containing ABP-dextran, processed for chemical analysis, or subjected to multiple investigations in tandem (see Methods). ***B)*** We covalently bound sulfate groups to algal biopolymer agarose and cast this as a gel in aCSF to model perineuronal interstitial matrix that is rich in chondroitin sulfate-decorated glycosaminoglycans. We compared sulfated agarose gel to native agar and agarose gels, achieving a 250-fold increase in sulfate content compared to commercially available agar (bar 3 vs bar 1, respectively; $p < 0.001$, Student's paired *t*-test; note discontinuous y-axis). Commercially available agarose, which is intended as a sulfate-free product, had no measurable sulfate content (bar 2) and subsequently was used as a control gel. ***C)*** Chloride concentration was reduced in sulfated agarose gels. Cl^- was measured using both a standard colorimetric assay (dark gray bars) and ABP-dextran FLIM (light gray bars) in aCSF control (leftmost pair), within non-sulfated agarose gel (center pair) and within sulfated agarose gel containing ≈50mM (49.2+/-0.289mM) covalently bound sulfate (rightmost pair). Measured chemically or using ABP-dextran FLIM, Cl^- in sulfated agarose gels differed significantly from aCSF ($p = 0.00264$ and $p < 0.001$, respectively) and non-sulfated agarose gels ($p = 0.00354$ and $p < 0.001$, respectively), while Cl^- measured in non-sulfated agarose gels was not significantly different from aCSF when measured by chemical assay ($p = 0.190$) but registered a small but significant difference (3.5% increased Cl- relative to aCSF, $p = 0.00328$) when measured with ABP-dextran FLIM, each compared using Student's paired *t*-test. ***D)*** Significant

chloride concentration differences between agarose gels with 50mM covalently bound sulfate (dark blue) and non-sulfated agarose gels (light blue) do not equilibrate with time but instead are stable for as long as experimentally observed (> 3 weeks). ANOVA testing with Bonferroni correction demonstrates that Cl^- significantly differs between native agarose and sulfated agarose at all time points (overall and each pair $p < 0.001$) while neither agarose (each $p = 1.0000$) nor sulfated agarose gels (from left to right, $p = 1.0000$; $p = 0.2119$; $p = 0.1129$) change significantly with time. ***E)*** Demonstration of stable juxtaposition of significantly different chloride concentrations at equilibrium. Separately cast sulfated and non-sulfated gel pieces are placed in a single vessel as described in ***A*** and equilibrated in common aCSF with ABP-dextran. Sulfated agarose gels (dark blue) again contain significantly lower Cl^- than do non-sulfated agarose gels (light blue; $p < 0.001$) or perfusate aCSF (gray; $p < 0.001$). Cl^- within non-sulfated agarose gels is again not significantly different than perfusate aCSF ($p = 0.0647$), all analyzed using Student's paired *t*-test. *Statistical significance indicated on graph for p-values <0.05 (*); <0.01 (**); <0.001 (***); "ns" indicates "not significant". Error bars reflect standard deviation from the mean.*

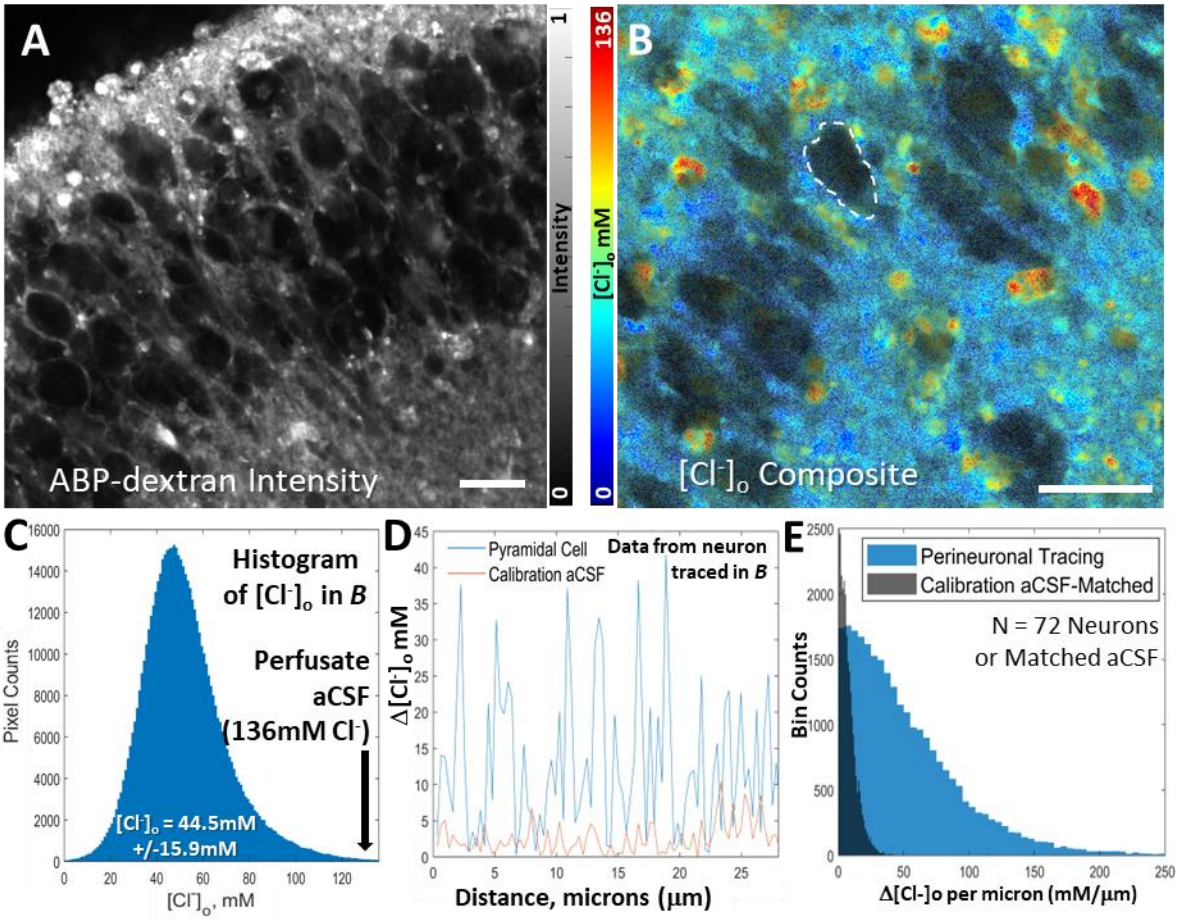

Figure 3 Cl^- in the extracellular space is not uniform and is considerably lower than aCSF perfusate. ***A)*** High-magnification HOSC intensity image of ABP-dextran excluded from cell bodies in the pyramidal cell layer (CA1; scale bar 20μm). ***B)*** Chloride-composite image again demonstrating the exclusion of ABP-dextran from intracellular spaces as well as the non-uniformity of Cl^-_o in the pyramidal cell layer of a representative HOSC. Representative pyramidal cell visible just above and left of image center, identified by ABP-dextran exclusion and morphology of resulting silhouette, is one of 6-10 neurons per field deemed to have a regular and nearly-continuous border analyzed as described in ***D&E*** (scale bar 20μm). ***C)*** Histogram of full field Cl^-_o in HOSC pictured in ***B***, demonstrating non-uniformity visually apparent in ***B***. Notably, Cl^-_o = 44.5+/-15.9mM despite perfusate $[Cl^-]$ = 136mM (across all depths of this slice Cl^-_o = 49.7+/-18.5mM; mean +/- SD). ***D)*** Change in chloride ($\Delta[Cl^-]_o$) plotted against distance in the perineuronal space (blue line) or the same trace overlaid onto a calibration aCSF FLIM image (red line) corresponding to the perineuronal trace in ***B***. $\Delta[Cl^-]_o$ of calibration aCSF (red) encapsulates machine and experimental noise, and $\Delta[Cl^-]_o$ in the perineuronal space (blue) exceeds that of control in this representative neuron. ***E)*** Perineuronal $\Delta[Cl^-]_o$ per micron calculated from many neurons' circumferential traces demonstrates that the variability of perineuronal Cl^-_o in living *in vitro* system exceeds the variability of control aCSF (72 neurons versus matched calibration aCSF controls from depths of 20-100μm in this representative HOSC). *Cl^-_o image rendering and presentation details can be found in Methods and in subsequent figures. Scale bars A&B: 20μm.*

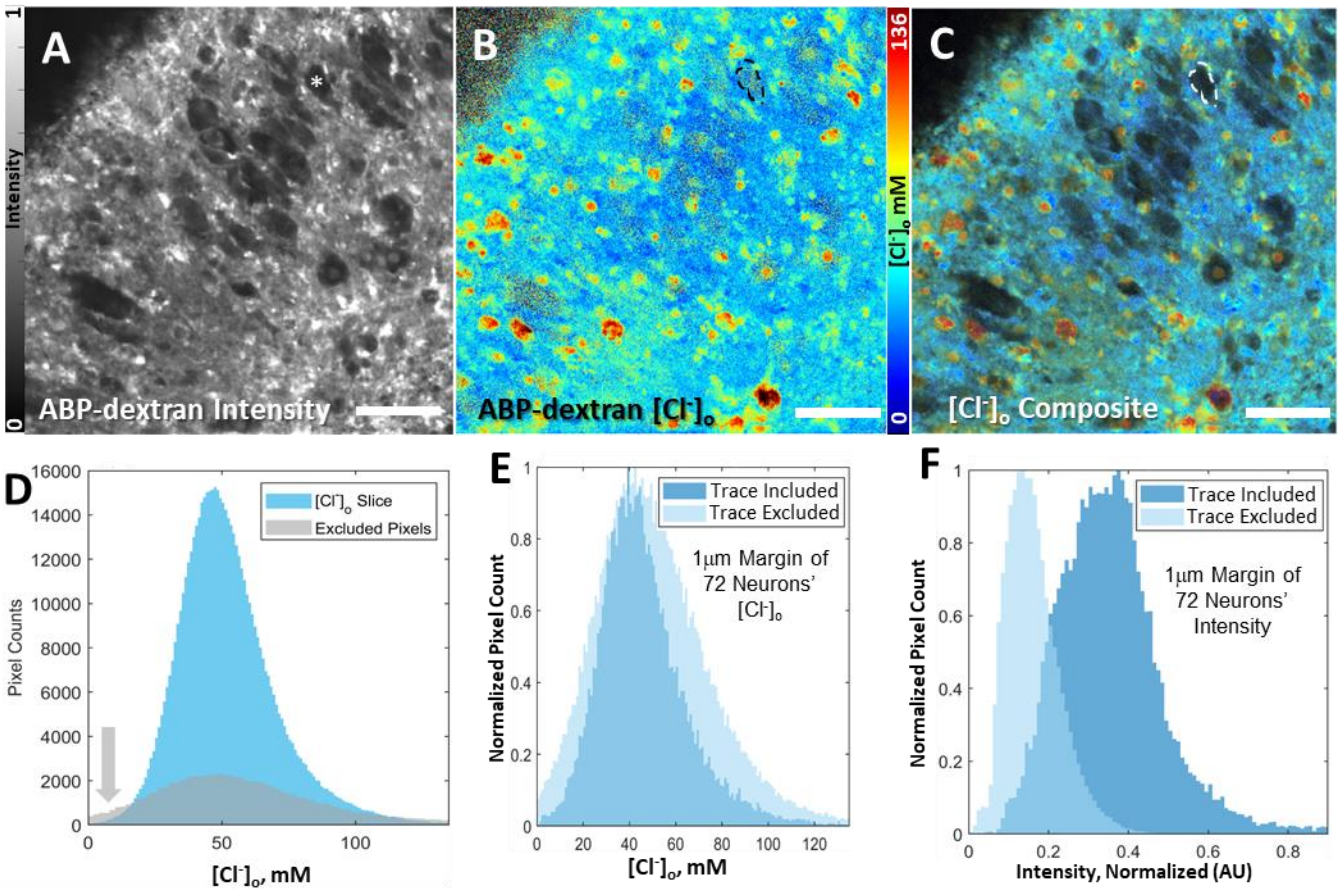

<u>Figure 4</u> Generation of composite chloride images and cell body masking for pixel quantification. ***A)*** ABP-dextran intensity data of an HOSC, derived by taking the total number of photons detected in each pixel throughout the acquisition period, is used to inform on tissue structure. Image series ***A-C*** corresponds to Figure 3B and its traced neuron example. Neuron silhouette traced in ***B&C*** is indicated with a white asterisk. ***B)*** Cl^-_o calculated from ABP-dextran lifetime. The loss of discernible structure is due to the fact that the intensity of the ABP-dextran signal has no effect on the Cl^-_o calculated from fluorescence lifetime (see Methods). Areas corresponding to cell body silhouettes in ***A*** have notable pixelation with relatively high apparent Cl^-_o values interspersed with black pixels, the latter indicating statistical exclusion due to low signal intensity (see Methods). ***C)*** In order to observe Cl^-_o with spatial context restored, we use intensity data to inform the brightness of the raw chloride data in ***B***, generating a composite image in which the color corresponds to Cl^-_o and brightness is attenuated based on the intensity of the signal in each pixel (see Methods). The most popular proprietary FLIM software packages use similar methods of composite data display. Note that prior to Cl^-_o analysis a further intensity-based thresholding step excludes pixels from inside somatic silhouettes in the focal plane, and pixels not corresponding to the slice (i.e., perfusate, top left) are also excluded by manually drawn ROI (masks not shown). ***D)*** Histogram of Cl^-_o in all analyzed pixels (blue) versus pixels excluded through thresholding step, principally marking somatic silhouettes (gray) in this representative HOSC, demonstrating no secondary peak at typical Cl^-_i values (i.e., =< 15mM). Further, this range of low Cl^-_o values is more likely excluded (gray) than included (blue) in our analysis (indicated by gray arrow). ***E&F)*** To further verify the cellular exclusion of ABP-dextran,

we looked specifically at the margins of well-defined somatic silhouettes, such as the example marked across ***A-C***, to search for signs of intracellular ABP-dextran leakage. We compared perineuronal pixels up to 1mm outside neurons to those pixels which lie inside the somatic margins of 72 neurons but were not excluded prior to thresholding (statistically excluded pixels are not considered; see Methods). Consistent with out-of-focus extracellular ABP-dextran, we found similar calculated Cl^-_o values between the two groups (***E***) with the expected wider variance in the less intense intracellular signal (***F***; see text). *Scale bar:* ***A-C*** *50μm.*

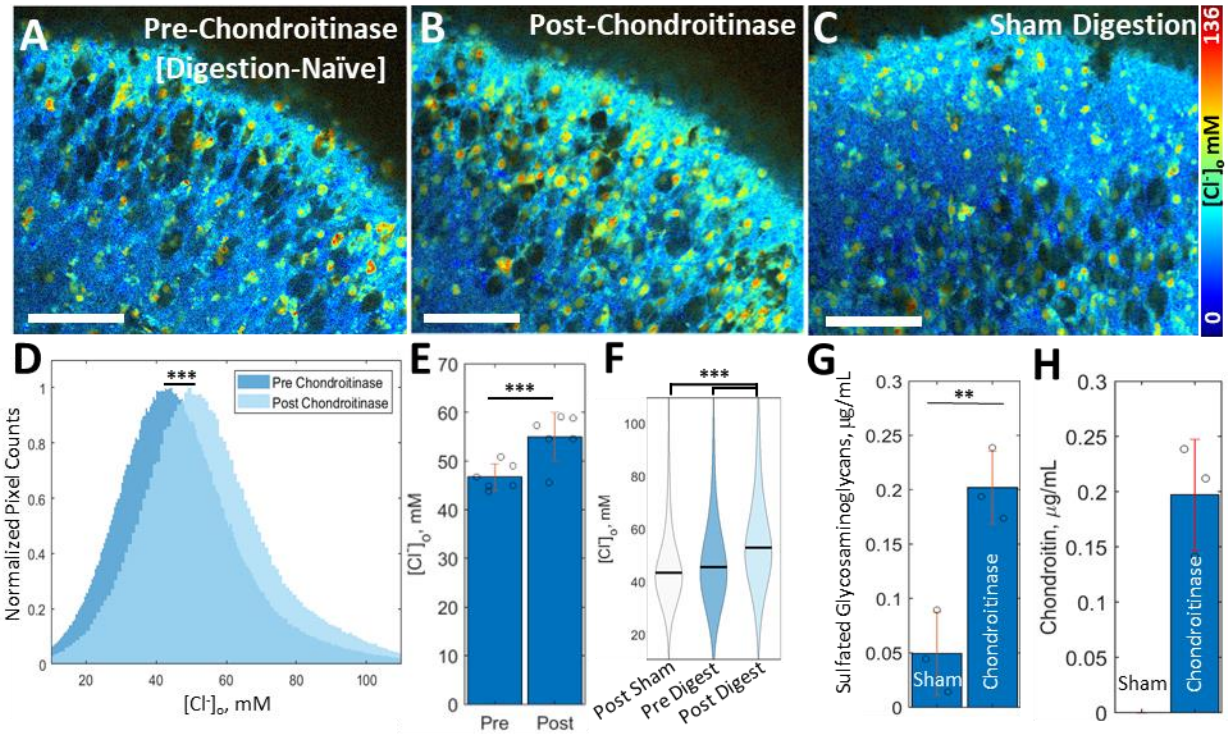

<u>Figure 5</u> Chondroitinase treatment removes fixed perineuronal anions and attenuates Cl^-_o displacement. Cl^-_o composite images of representative mouse hippocampus slice cultures imaged in culture media (Cl^- ≈ 64mM) with 1mg/mL ABP-dextran (100mM ABP-Dextran) before (***A***) and after (***B***) treatment with bacterial MMP analog chondroitinase, or after sham digestion (***C***); shared colorbar for ***A-C*** at right. ***D)*** Histograms of $[Cl^-]_o$ corresponding to ***A&B*** demonstrate pre-chondroitinase digestion (dark blue) and post-chondroitinase digestion (light blue) $[Cl^-]_o$ populations of pixels are significantly different ($p < 0.001$ by Kolmogorov-Smirnov paired-sample test). ***E)*** When images from ***A&B*** are broken into regularly shaped regions of interest and analyzed as paired groups, pre-chondroitinase and post-chondroitinase are again significantly different (46.7+/-2.7mM vs 55.0+/- 5.0mM, respectively, mean+/-SD; $p = 0.00523$ by Student's paired *t*-test). ***F)*** Violin plot of data from ***A&B*** (dark and light blue, respectively) vs grouped sham-digested slice data (gray) demonstrating that Cl^-_o increases significantly after chondroitin sulfate is removed by digestion, whether compared to pre-digestion of the same slice or a sham digestion (each $p < 0.001$ by Kolmogorov-Smirnov paired-sample test). ***G)*** Measurement of glycosaminoglycans, including chondroitin sulfate, released into the perfusate after HOSCs are treated with chondroitinase (vs sham digestion) using a commercial colorimetric assay. A significantly higher concentration of polyanionic glycosaminoglycans are found in the extracellular fluid after chondroitinase digestion ($p = 0.00632$ by Student's paired *t*-test), consistent with the release of chondroitin sulfate from extracellular matrix within slice cultures and a resultant increase in Cl^-_o. ***H)*** HPLC analysis confirms the presence of chondroitin sulfate released into digestion buffer after chondroitinase treatment (mean = 0.20μg/mL); there was no detectable chondroitin sulfate in sham digests, negating formal significance testing. ***A-C*** *scale bars 50μm; all slice cultures were DIV14-21 at time of experiment; cultures were grown directly on glass with the exception of* ***G*** *where cultures were grown on membrane inserts (see Methods); significance values noted graphically for p-values <0.05 (*); <0.01 (**); <0.001 (***);*

*“ns” indicates “not significant”. Note that data contained in **D-F** labeled ‘pre’ and ‘post’ are derived from HOSCs in **A** and **B**, respectively.*

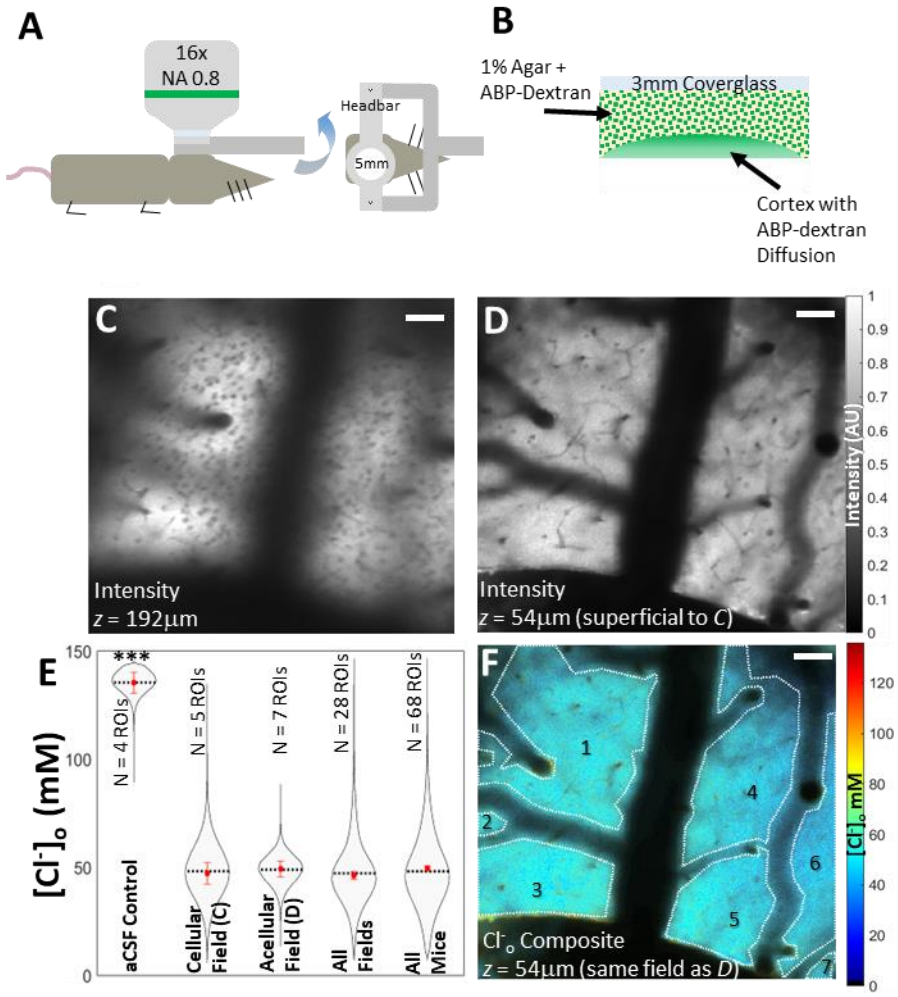

<u>Figure 6 *In vivo* Cl^-_o in mouse neocortex is consistent with *ex vivo* findings.</u> ***A&B)*** Schematic of *in vivo* imaging set-up, using a surgically implanted headbar to immobilize P26-P30 mouse pup for imaging through 3mm coverglass window overlaying 1% agar brought up in aCSF containing ABP-Dextran and 136mM chloride laid directly on exposed cortex. ***C)*** Intensity image of mouse L2/3 cortex, demonstrating ABP-dextran exclusion from cells and vessels; large vessels appear blurred because their widest diameter exists superficial to this field (depth 192µm). ***D)*** Chloride composite image corresponding to L1 cortex 138µm superficial to field ***C*** (depth 54µm). ***E)*** Cl^-_o in mouse neocortex is significantly lower than the CSF Cl^- as shown in this violin plot of all ROI pixels with population mean (black dashed lines) and overlaid mean+/-standard error of ROIs analyzed. Compared to agarose brought up in 136mM aCSF overlying the cortex (leftmost violin plot: 135.4+/-5.0mM; mean+/-standard deviation of all analyzed pixels), *in vivo* mouse cortex had significantly lower Cl^-_o whether measured in cellular fields such as in ***C*** or in acellular fields such as in ***D*** (plots 2 and 3: 48.9+/-6.7mM and 55.0+/-17.9mM, respectively). This was true when considering all ROIs in all fields from the animal from which ***C&D*** were taken (plot 4: 47.2+/-14.9mM), and when considering all fields from all animals used in this study (plot 5: 48.1+/-17.0mM). Statistically comparing discreet ROI means by ANOVA analysis with Bonferroni correction (red overlay indicating mean+/-standard error of ROIs), all groups demonstrated a statistically significant difference vs control ($p < 0.001$) but were not

significantly different vs each other (p = 1.0000). Note that ROIs are too numerous to display for all groups, and we have instead overlaid the mean+/-standard error (red lines) associated with ANOVA analysis of ROIs. Violin plot means (dashed black lines), reflecting aggregated pixels from all ROIs, appear on the graph; associated standard deviations are listed above but are not explicitly labeled on graph. ***F)*** Region of interest (ROI) selection example with ROIs shown numbered in Cl^-_o composite image, corresponding to intensity image in ***D***, demonstrates exclusion of large vessels but is otherwise permissive. *Scale bars* ***C,D&F****: 50μm; significance values noted graphically for p-values <0.05 (*); <0.01 (**); <0.001 (***); "ns" indicates "not significant".*

.

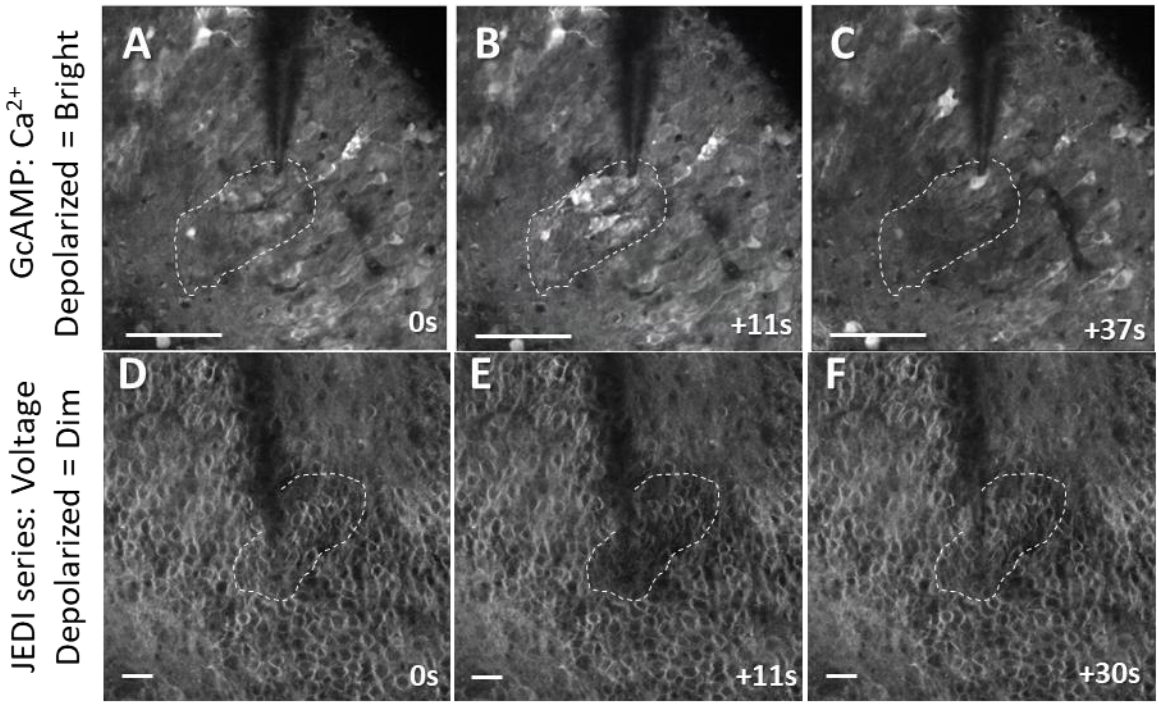

<u>Supplemental Figure 1</u>: Evidence for pipette effects on local extracellular environment. CA1 pyramidal cells in HOSCs can be seen to depolarize due to leakage of internal solution from patch pipette containing 150mM KCl. Whether an area of pyramidal cells become bright due to depolarization, as is the case in neurons expressing GcAMP ***(A-C)***, or dim due to depolarization, as is the case in neurons expressing JEDI-series voltage-sensitive system (Liu *et al.*, 2022) ***(D-F)***, depolarization in response to high K^+ occurs in the vicinity of the pipette tip (white dashed line). Neurons generally recover soon after a seal is achieved, precluding further leakage and/or diffusion of internal solution from the pipette electrode. *Scale bars: 50μm*.

Bibliography

Alger BE & Nicoll RA. (1982). Pharmacological evidence for two kinds of GABA receptor on rat hippocampal pyramidal cells studied in vitro. *J Physiol* **328,** 125-141.

Barker JL & Ransom BR. (1978). Amino acid pharmacology of mammalian central neurones grown in tissue culture. *J Physiol* **280,** 331-354.

Beckstein O & Naughton F. (2022). General principles of secondary active transporter function. *Biophys Rev (Melville)* **3,** 011307.

Berdichevsky Y, Saponjian Y, Park KI, Roach B, Pouliot W, Lu K, Swiercz W, Dudek FE & Staley KJ. (2016). Staged anticonvulsant screening for chronic epilepsy. *Ann Clin Transl Neurol* **3,** 908-923.

Biwersi J, Farah N, Wang Y-X, Ketcham R & Verkman A. (1992a). Synthesis of cell-impermeable Cl- sensitive fluorescent indicators with improved sensitivity and optical properties. *American Journal of Physiology-Cell Physiology* **262,** C243-C250.

Biwersi J, Farah N, Wang YX, Ketcham R & Verkman AS. (1992b). Synthesis of cell-impermeable Cl- sensitive fluorescent indicators with improved sensitivity and optical properties. *Am J Physiol* **262,** C242-250.

Biwersi J, Tulk B & Verkman AS. (1994). Long-wavelength chloride-sensitive fluorescent indicators. *Anal Biochem* **219,** 139-143.

Brumback AC & Staley KJ. (2008). Thermodynamic regulation of NKCC1-mediated Cl- cotransport underlies plasticity of GABA(A) signaling in neonatal neurons. *J Neurosci* **28,** 1301-1312.

Celio MR & Blümcke I. (1994). Perineuronal nets--a specialized form of extracellular matrix in the adult nervous system. *Brain Res Brain Res Rev* **19,** 128-145.

Celio MR, Spreafico R, De Biasi S & Vitellaro-Zuccarello L. (1998). Perineuronal nets: past and present. *Trends Neurosci* **21,** 510-515.

Chahine NO, Chen FH, Hung CT & Ateshian GA. (2005). Direct measurement of osmotic pressure of glycosaminoglycan solutions by membrane osmometry at room temperature. *Biophys J* **89,** 1543-1550.

Che A & De Marco García NV. (2021). An in vivo Calcium Imaging Approach for the Identification of Cell-Type Specific Patterns in the Developing Cortex. *Front Neural Circuits* **15,** 747724.

Cohen I, Navarro V, Clemenceau S, Baulac M & Miles R. (2002). On the origin of interictal activity in human temporal lobe epilepsy in vitro. *Science* **298,** 1418-1421.

Coombs JS, Eccles JC & Fatt P. (1955). The specific ionic conductances and the ionic movements across the motoneuronal membrane that produce the inhibitory post-synaptic potential. *J Physiol* **130,** 326-374.

DiRaddo JO, Miller EJ, Bowman-Dalley C, Wroblewska B, Javidnia M, Grajkowska E, Wolfe BB, Liotta DC & Wroblewski JT. (2015). Chloride is an Agonist of Group II and III Metabotropic Glutamate Receptors. *Mol Pharmacol* **88,** 450-459.

Doyon N, Vinay L, Prescott SA & De Koninck Y. (2016). Chloride regulation: a dynamic equilibrium crucial for synaptic inhibition. *Neuron* **89,** 1157-1172.

Düsterwald KM, Currin CB, Burman RJ, Akerman CJ, Kay AR & Raimondo JV. (2018). Biophysical models reveal the relative importance of transporter proteins and impermeant anions in chloride homeostasis. *Elife* **7**.

Ebihara S, Shirato K, Harata N & Akaike N. (1995). Gramicidin-perforated patch recording: GABA response in mammalian neurones with intact intracellular chloride. *J Physiol* **484 (Pt 1),** 77-86.

Egawa K, Yamada J, Furukawa T, Yanagawa Y & Fukuda A. (2013). Cl^- homeodynamics in gap junction-coupled astrocytic networks on activation of GABAergic synapses. *J Physiol* **591,** 3901-3917.

Epsztein R, Shaulsky E, Dizge N, Warsinger DM & Elimelech M. (2018). Role of Ionic Charge Density in Donnan Exclusion of Monovalent Anions by Nanofiltration. *Environ Sci Technol* **52,** 4108-4116.

Fatin-Rouge N, Milon A, Buffle J, Goulet RR & Tessier A. (2003). Diffusion and partitioning of solutes in agarose hydrogels: the relative influence of electrostatic and specific interactions. *The Journal of Physical Chemistry B* **107,** 12126-12137.

Florence TM & Farrar YJ. (1971). Spectrophotometric determination of chloride at the parts-per-billion level by the mercury(II) thiocyanate method. *Analytica chimica acta* **54,** 373--377.

Frantz C, Stewart KM & Weaver VM. (2010). The extracellular matrix at a glance. *J Cell Sci* **123,** 4195-4200.

Fuse T & Toshiya S. (1975). Preparation and properties of agar sulfates. *Agricultural and biological chemistry* **39,** 119--126.

1029 Gao KW, Yu X, Darling RM, Newman J & Balsara NP. (2022). Increased Donnan exclusion in charged
1030 polymer networks at high salt concentrations. *Soft Matter* **18,** 282-292.

1031

1032 Gehlen MH. (2020). The centenary of the Stern-Volmer equation of fluorescence quenching: From the
1033 single line plot to the SV quenching map. *Journal of photochemistry and photobiology C,*
1034 *Photochemistry reviews* **42,** 100338.

1035

1036 Glykys J, Dzhala V, Egawa K, Balena T, Saponjian Y, Kuchibhotla K, Bacskai B, Kahle K, Zeuthen T & Staley
1037 K. (2014a). Local impermeant anions establish the neuronal chloride concentration. *Science* **343,**
1038 670-675.

1039

1040 Glykys J, Dzhala V, Egawa K, Balena T, Saponjian Y, Kuchibhotla KV, Bacskai BJ, Kahle KT, Zeuthen T &
1041 Staley KJ. (2014b). Response to comments on "Local impermeant anions establish the neuronal
1042 chloride concentration". *Science* **345,** 1130.

1043

1044 Glykys J, Dzhala V, Egawa K, Kahle KT, Delpire E & Staley K. (2017). Chloride dysregulation, seizures, and
1045 cerebral edema: a relationship with therapeutic potential. *Trends in neurosciences* **40,** 276-294.

1046

1047 Golgi C. (1898). Intomo alla struttura delle cellule nervose. *Boll Soc Med-Chir Pavia* **1,** 1-14.

1048

1049 González MI. (2016). Regulation of the cell surface expression of chloride transporters during
1050 epileptogenesis. *Neurosci Lett* **628,** 213-218.

1051

1052 Gregor HP. (1951). Gibbs-Donnan equilibria in ion exchange resin systems. *Journal of the American*
1053 *Chemical Society* **73,** 642-650.

1054

1055 Grimley JS, Li L, Wang W, Wen L, Beese LS, Hellinga HW & Augustine GJ. (2013a). Visualization of
1056 synaptic inhibition with an optogenetic sensor developed by cell-free protein engineering
1057 automation. *J Neurosci* **33,** 16297-16309.

1058

1059 Grimley JS, Li L, Wang W, Wen L, Beese LS, Hellinga HW & Augustine GJ. (2013b). Visualization of
1060 synaptic inhibition with an optogenetic sensor developed by cell-free protein engineering
1061 automation. *Journal of Neuroscience* **33,** 16297-16309.

1062

1063 Hampe CS, Eisengart JB, Lund TC, Orchard PJ, Swietlicka M, Wesley J & McIvor RS. (2020).
1064 Mucopolysaccharidosis Type I: A Review of the Natural History and Molecular Pathology. *Cells* **9**.

1065

1066 Helfferich F. (1995). *Ion Exchange*. Dover, New York, NY.

1067

1068 Hu H, Gan J & Jonas P. (2014). Interneurons. Fast-spiking, parvalbumin^{+} GABAergic interneurons: from
1069 cellular design to microcircuit function. *Science* **345,** 1255263.

1070
1071 Huberfeld G, Wittner L, Clemenceau S, Baulac M, Kaila K, Miles R & Rivera C. (2007). Perturbed chloride
1072 homeostasis and GABAergic signaling in human temporal lobe epilepsy. *J Neurosci* **27,** 9866-
1073 9873.

1074
1075 Huguenard JR & Alger BE. (1986). Whole-cell voltage-clamp study of the fading of GABA-activated
1076 currents in acutely dissociated hippocampal neurons. *J Neurophysiol* **56,** 1-18.

1077
1078 Héron B, Mikaeloff Y, Froissart R, Caridade G, Maire I, Caillaud C, Levade T, Chabrol B, Feillet F, Ogier H,
1079 Valayannopoulos V, Michelakakis H, Zafeiriou D, Lavery L, Wraith E, Danos O, Heard JM &
1080 Tardieu M. (2011). Incidence and natural history of mucopolysaccharidosis type III in France and
1081 comparison with United Kingdom and Greece. *Am J Med Genet A* **155a,** 58-68.

1082
1083 Jedlicka P, Deller T, Gutkin BS & Backus KH. (2011). Activity-dependent intracellular chloride
1084 accumulation and diffusion controls GABA(A) receptor-mediated synaptic transmission.
1085 *Hippocampus* **21,** 885-898.

1086
1087 Jha RM, Kochanek PM & Simard JM. (2019). Pathophysiology and treatment of cerebral edema in
1088 traumatic brain injury. *Neuropharmacology* **145,** 230-246.

1089
1090 Jiang C, Agulian S & Haddad GG. (1992). Cl- and Na+ homeostasis during anoxia in rat hypoglossal
1091 neurons: intracellular and extracellular in vitro studies. *J Physiol* **448,** 697-708.

1092
1093 Kaneko H, Putzier I, Frings S, Kaupp UB & Gensch T. (2004). Chloride accumulation in mammalian
1094 olfactory sensory neurons. *J Neurosci* **24,** 7931-7938.

1095
1096 Karamanos NK, Theocharis AD, Piperigkou Z, Manou D, Passi A, Skandalis SS, Vynios DH, Orian-Rousseau
1097 V, Ricard-Blum S, Schmelzer CEH, Duca L, Durbeej M, Afratis NA, Troeberg L, Franchi M, Masola
1098 V & Onisto M. (2021). A guide to the composition and functions of the extracellular matrix. *Febs*
1099 *j* **288,** 6850-6912.

1100
1101 Karlócai MR, Wittner L, Tóth K, Maglóczky Z, Katarova Z, Rásonyi G, Erőss L, Czirják S, Halász P, Szabó G,
1102 Payne JA, Kaila K & Freund TF. (2016). Enhanced expression of potassium-chloride cotransporter
1103 KCC2 in human temporal lobe epilepsy. *Brain Struct Funct* **221,** 3601-3615.

1104
1105 Kroeger D, Tamburri A, Amzica F & Sík A. (2010). Activity-dependent layer-specific changes in the
1106 extracellular chloride concentration and chloride driving force in the rat hippocampus. *J*
1107 *Neurophysiol* **103,** 1905-1914.

1108
1109 Kuang D & Hampson DR. (2006). Ion dependence of ligand binding to metabotropic glutamate receptors.
1110 *Biochem Biophys Res Commun* **345,** 1-6.

1111
1112 Kuner T & Augustine GJ. (2000). A genetically encoded ratiometric indicator for chloride: capturing
1113 chloride transients in cultured hippocampal neurons. *Neuron* **27,** 447-459.

1114
1115 Kusama N, Harding AM & Benson CJ. (2010). Extracellular chloride modulates the desensitization
1116 kinetics of acid-sensing ion channel 1a (ASIC1a). *J Biol Chem* **285,** 17425-17431.

1117
1118 Lawrence R, Olson SK, Steele RE, Wang L, Warrior R, Cummings RD & Esko JD. (2008). Evolutionary
1119 differences in glycosaminoglycan fine structure detected by quantitative glycan reductive
1120 isotope labeling. *J Biol Chem* **283,** 33674-33684.

1121
1122 Lesperance LM, Gray ML & Burstein D. (1992). Determination of fixed charge density in cartilage using
1123 nuclear magnetic resonance. *J Orthop Res* **10,** 1-13.

1124
1125 Lewin N, Aksay E & Clancy CE. (2012). Computational modeling reveals dendritic origins of GABA(A)-
1126 mediated excitation in CA1 pyramidal neurons. *PLoS One* **7,** e47250.

1127
1128 Li M, Toombes GE, Silberberg SD & Swartz KJ. (2015). Physical basis of apparent pore dilation of ATP-
1129 activated P2X receptor channels. *Nat Neurosci* **18,** 1577-1583.

1130
1131 Liu Z, Lu X, Villette V, Gou Y, Colbert KL, Lai S, Guan S, Land MA, Lee J, Assefa T, Zollinger DR, Korympidou
1132 MM, Vlasits AL, Pang MM, Su S, Cai C, Froudarakis E, Zhou N, Patel SS, Smith CL, Ayon A,
1133 Bizouard P, Bradley J, Franke K, Clandinin TR, Giovannucci A, Tolias AS, Reimer J, Dieudonné S &
1134 St-Pierre F. (2022). Sustained deep-tissue voltage recording using a fast indicator evolved for
1135 two-photon microscopy. *Cell* **185,** 3408-3425.e3429.

1136
1137 Margolis RK & Margolis RU. (1973). The turnover of hexosamine and sialic acid in glycoproteins and
1138 mucopolysaccharides of brain. *Biochim Biophys Acta* **304,** 413-420.

1139
1140 Marinsky JA. (1985a). An interpretation of the sensitivity of weakly acidic (basic) polyelectrolyte (cross-
1141 linked and linear) equilibria to excess neutral salt. *Journal of physical chemistry (1952)* **89,** 5294--
1142 5302.

1143
1144 Marinsky JA. (1985b). An interpretation of the sensitivity of weakly acidic (basic) polyelectrolyte (cross-
1145 linked and linear) equilibria to excess neutral salt. *The Journal of Physical Chemistry* **89,** 5294-
1146 5302.

1147
1148 Morawski M, Reinert T, Meyer-Klaucke W, Wagner FE, Tröger W, Reinert A, Jäger C, Brückner G &
1149 Arendt T. (2015). Ion exchanger in the brain: quantitative analysis of perineuronally fixed anionic
1150 binding sites suggests diffusion barriers with ion sorting properties. *Scientific reports* **5,** 16471.

1151

1152 Normoyle KP, Lillis KP & Staley KJ. (2024). Synthesis and Characterization of a Novel Concentration-
1153 Independent Fluorescent Chloride Indicator, ABP-Dextran, Optimized for Extracellular Chloride
1154 Measurement. *Biomolecules* **14**.

1155
1156 Orlando C, Ster J, Gerber U, Fawcett JW & Raineteau O. (2012). Perisynaptic chondroitin sulfate
1157 proteoglycans restrict structural plasticity in an integrin-dependent manner. *J Neurosci* **32,**
1158 18009-18017, 18017a.

1159
1160 Plested AJ & Mayer ML. (2007). Structure and mechanism of kainate receptor modulation by anions.
1161 *Neuron* **53,** 829-841.

1162
1163 Rahmati N, Normoyle KP, Glykys J, Dzhala VI, Lillis KP, Kahle KT, Raiyyani R, Jacob T & Staley KJ. (2021).
1164 Unique Actions of GABA Arising from Cytoplasmic Chloride Microdomains. *J Neurosci* **41,** 4957-
1165 4975.

1166
1167 Rasmussen MK, Mestre H & Nedergaard M. (2022). Fluid transport in the brain. *Physiol Rev* **102,** 1025-
1168 1151.

1169
1170 Reuter D, Zierold K, Schröder WH & Frings S. (1998). A depolarizing chloride current contributes to
1171 chemoelectrical transduction in olfactory sensory neurons in situ. *J Neurosci* **18,** 6623-6630.

1172
1173 Roll L & Faissner A. (2014). Influence of the extracellular matrix on endogenous and transplanted stem
1174 cells after brain damage. *Front Cell Neurosci* **8,** 219.

1175
1176 Sato SS, Artoni P, Landi S, Cozzolino O, Parra R, Pracucci E, Trovato F, Szczurkowska J, Luin S & Arosio D.
1177 (2017). Simultaneous two-photon imaging of intracellular chloride concentration and pH in
1178 mouse pyramidal neurons in vivo. *Proceedings of the National Academy of Sciences* **114,** E8770-
1179 E8779.

1180
1181 Seo JH, Okuyama T, Shapiro E, Fukuhara Y & Kosuga M. (2020). Natural history of cognitive development
1182 in neuronopathic mucopolysaccharidosis type II (Hunter syndrome): Contribution of genotype to
1183 cognitive developmental course. *Mol Genet Metab Rep* **24,** 100630.

1184
1185 Sidharthan NP, Minchin RF & Butcher NJ. (2013). Cytosolic sulfotransferase 1A3 is induced by dopamine
1186 and protects neuronal cells from dopamine toxicity: role of D1 receptor-N-methyl-D-aspartate
1187 receptor coupling. *J Biol Chem* **288,** 34364-34374.

1188
1189 Sola M, Kneussel M, Heck IS, Betz H & Weissenhorn W. (2001). X-ray crystal structure of the trimeric N-
1190 terminal domain of gephyrin. *J Biol Chem* **276,** 25294-25301.

1191

Song I & Dityatev A. (2018). Crosstalk between glia, extracellular matrix and neurons. *Brain Res Bull* **136,** 101-108.

Staley K. (2023). Ionic mechanisms of ictogenic disinhibition. In *Jasper's Basic Mechanisms of the Epilepsies*. In Press.

Staley KJ & Mody I. (1992). Shunting of excitatory input to dentate gyrus granule cells by a depolarizing GABAA receptor-mediated postsynaptic conductance. *J Neurophysiol* **68,** 197-212.

Staley KJ & Proctor WR. (1999). Modulation of mammalian dendritic GABA(A) receptor function by the kinetics of Cl- and HCO3- transport. *J Physiol* **519 Pt 3,** 693-712.

Staley KJ, Soldo BL & Proctor WR. (1995). Ionic mechanisms of neuronal excitation by inhibitory GABAA receptors. *Science* **269,** 977-981.

Stoppini L, Buchs PA & Muller D. (1991). A simple method for organotypic cultures of nervous tissue. *J Neurosci Methods* **37,** 173-182.

Syková E & Nicholson C. (2008). Diffusion in brain extracellular space. *Physiol Rev* **88,** 1277-1340.

Thom M. (2014). Review: Hippocampal sclerosis in epilepsy: a neuropathology review. *Neuropathol Appl Neurobiol* **40,** 520-543.

Thompson SM, Deisz RA & Prince DA. (1988). Relative contributions of passive equilibrium and active transport to the distribution of chloride in mammalian cortical neurons. *J Neurophysiol* **60,** 105-124.

Titze J, Shakibaei M, Schafflhuber M, Schulze-Tanzil G, Porst M, Schwind KH, Dietsch P & Hilgers KF. (2004). Glycosaminoglycan polymerization may enable osmotically inactive Na+ storage in the skin. *Am J Physiol Heart Circ Physiol* **287,** H203-208.

Tora AS, Rovira X, Cao AM, Cabayé A, Olofsson L, Malhaire F, Scholler P, Baik H, Van Eeckhaut A, Smolders I, Rondard P, Margeat E, Acher F, Pin JP & Goudet C. (2018). Chloride ions stabilize the glutamate-induced active state of the metabotropic glutamate receptor 3. *Neuropharmacology* **140,** 275-286.

Torres PB, Nagai A, Jara CEP, Santos JP, Chow F & dos Santos DYAC. (2021). Determination of sulfate in algal polysaccharide samples: a step-by-step protocol using microplate reader. *Ocean and Coastal Research* **69**.

1232 Tremblay R, Lee S & Rudy B. (2016). GABAergic Interneurons in the Neocortex: From Cellular Properties
1233 to Circuits. *Neuron* **91,** 260-292.

1234
1235 Tsien RY. (2013). Very long-term memories may be stored in the pattern of holes in the perineuronal
1236 net. *Proc Natl Acad Sci U S A* **110,** 12456-12461.

1237
1238 Tyzio R, Minlebaev M, Rheims S, Ivanov A, Jorquera I, Holmes GL, Zilberter Y, Ben-Ari Y & Khazipov R.
1239 (2008). Postnatal changes in somatic γ-aminobutyric acid signalling in the rat hippocampus.
1240 *European Journal of Neuroscience* **27,** 2515-2528.

1241
1242 Tønnesen J, Inavalli V & Nägerl UV. (2018). Super-Resolution Imaging of the Extracellular Space in Living
1243 Brain Tissue. *Cell* **172,** 1108-1121.e1115.

1244
1245 Urban JP, Maroudas A, Bayliss MT & Dillon J. (1979). Swelling pressures of proteoglycans at the
1246 concentrations found in cartilaginous tissues. *Biorheology* **16,** 447-464.

1247
1248 Verkman AS. (1990). Development and biological applications of chloride-sensitive fluorescent
1249 indicators. *Am J Physiol* **259,** C375-388.

1250
1251 Voipio J, Boron WF, Jones SW, Hopfer U, Payne JA & Kaila K. (2014). Comment on "Local impermeant
1252 anions establish the neuronal chloride concentration". *Science* **345,** 1130.

1253
1254 Xiao F, Nicholson C, Hrabe J & Hrabetová S. (2008). Diffusion of flexible random-coil dextran polymers
1255 measured in anisotropic brain extracellular space by integrative optical imaging. *Biophys J* **95,**
1256 1382-1392.

1257
1258 Zhang S, Kojic L, Tsang M, Grewal P, Liu J, Namjoshi D, Wellington CL, Tetzlaff W, Cynader MS & Jia W.
1259 (2016). Distinct roles for metalloproteinases during traumatic brain injury. *Neurochem Int* **96,**
1260 46-55.

1261
1262 Zhang YW, Uchendu S, Leone V, Bradshaw RT, Sangwa N, Forrest LR & Rudnick G. (2021). Chloride-
1263 dependent conformational changes in the GlyT1 glycine transporter. *Proc Natl Acad Sci U S A*
1264 **118**.

1265

1266

1267

Additional Information:

Competing Interests: None of the authors have any competing interests to declare, as indicated during the submission process for each author individually.

Funding: This work was funded by two grants to Kevin J. Staley from the National Institute for Neurological Disorders and Stroke (NINDS): R35 NS116852 and P01 NS127769.

Data availability statement: All data files used to generate the figures in the paper can be found on GitHub under KieranNormoyle/NeuronalChloride2023. Please note that the authors are still working to compile and upload data files as of article submission, but these will be ready prior to publication.

Authors' Translational Perspective: We hypothesized that if measured non-invasively, the extracellular chloride concentration (Cl^-_o) would be less than CSF chloride values (≈110mM) due to Donnan exclusion by heterogeneously distributed extracellular anions so that Cl^-_o would be lower than expected and heterogenous. We found that Cl^-_o has a mean value much lower than previously appreciated (≈50mM) and is indeed heterogenous. Our data further demonstrates that the loss of heterogenous sulfated glycosaminoglycans (sGAGs) in extracellular matrix results in an increased Cl^-_o as the Donnan equilibrium rebalances. Together with our previous work demonstrating heterogenous intracellular chloride (Cl^-_i), our data suggests the variance of GABA reversal potential (E_{GABA}) we and others have observed is due to the heterogeneity of the concentrations of the primary permeant anion, Cl^-, on both the intra- and extracellular side of the channel. Stable variations of perisynaptic Cl^-_o or Cl^-_i potentially allows for the tuning of E_{GABA} at individual $GABA_A$ synapses and suggests a mechanism for information storage. Pathophysiological alteration of Cl^-_o would be expected to occur when sGAG-containing extracellular matrix is damaged, such as when matrix metalloproteases (MMPs) are released following neuronal injury or death. The expected increase in extracellular chloride salts, in turn leading to equilibrative intracellular increases, represents a new mechanism of cytotoxic edema.